Vol. 92 No. 1 pp. 106–126 ACTA GEOLOGICA SINICA (English Edition) Feb. 2018

Geochronology, Geochemistry and Sr-Nd-Pb-Hf Isotopes of No. I Complex from the Shitoukengde Ni–Cu Sulfide Deposit in the Eastern Kunlun Orogen, Western China: Implications for the Magmatic Source, Geodynamic Setting and Genesis

LI Liang[1], SUN Fengyue[1,*], LI Bile[1], LI Shijin[2], CHEN Guangjun[1], WANG Wei[2], YAN Jiaming[1], ZHAO Tuofei[1], DONG Jun[3] and ZHANG Dexin[2]

1 *College of Earth Sciences, Jilin University, Changchun 130061, China*
2 *Qinghai Bureau of Geological Survey, Xining 810001, China*
3 *No. 108 Geological Party, Sichuan Bureau of Geology and Mineral Exploration, Chengdu 611230, China*

Abstract: The Shitoukengde Ni-Cu deposit, located in the Eastern Kunlun Orogen, comprises three mafic–ultramafic complexes, with the No. I complex hosting six Ni-Cu orebodies found recently. The deposit is hosted in the small ultramafic bodies intruding Proterozoic metamorphic rocks. Complexes at Shitoukengde contain all kinds of mafic-ultramafic rocks, and olivine websterite and pyroxene peridotite are the most important Ni-Cu-hosted rocks. Zircon U-Pb dating suggests that the Shitoukengde Ni-Cu deposit formed in late Silurian (426–422 Ma), and their zircons have $\varepsilon_{Hf}(t)$ values of −9.4 to 5.9 with the older T_{DM1} ages (0.80–1.42 Ga). Mafic-ultramafic rocks from the No. I complex show the similar rare earth and trace element patterns, which are enriched in light rare earth elements and large ion lithophile elements (e.g., K, Rb, Th) and depleted in heavy rare earth elements and high field strength elements (e.g., Ta, Nb, Zr, Ti). Sulfides from the deposit have the slightly higher $\delta^{34}S$ values of 1.9–4.3‰ than the mantle (0 ± 2‰). The major and trace element characteristics, and Sr-Nd-Pb and Hf, S isotopes indicate that their parental magmas originated from a metasomatised, asthenospheric mantle source which had previously been modified by subduction-related fluids, and experienced significant crustal contamination both in the magma chamber and during ascent triggering S oversaturation by addition of S and Si, that resulted in the deposition and enrichment of sulfides. Combined with the tectonic evolution, we suggest that the Shitoukengde Ni-Cu deposit formed in the post-collisional, extensional regime related to the subducted oceanic slab break-off after the Wanbaogou oceanic basalt plateau collaged northward to the Qaidam Block in late Silurian.

Key words: Sr-Nd-Pb-Hf isotopes, crustal contamination, oceanic slab break-off, post-collisional extension, Shitoukengde Ni-Cu deposit, Eastern Kunlun Orogen

1 Introduction

Many magmatic Ni–Cu sulfide deposits associated with small-scale (~1 km^2) ultramafic intrusion in orogenic belt have been discovered in Xinjiang Province (Huangshan, Wang Chongyi et al., 1986; Huangshandong, Ni Zhiyao, 1991; Kelatongke, Zhang Zhaochong et al., 2003; Zhang et al., 2009a; Tulaergen, Sun He et al., 2006; Jiao Jiangang et al., 2012; Fu Piaoer et al., 2012; Huangshannan, Zhao Yun et al., 2016), Qinghai Province (Xiarihamu; Li Shijin et al., 2012; Wang Guan et al., 2014a; Peng et al., 2016) and Jilin Province (Hongqiling; Lu Linsu et al., 2012; Wei et al., 2013) of China, and they have been the focus of several studies in recent years. Such deposits typically form from pulses of magma injection and are extensively mineralized. Tang Zhongli et al. (1991) suggested that several such small intrusions combine to form large deposits, and tectonic models have been proposed for the formation of magmatic Ni–Cu sulfide deposits in China (Tang Zhongli et al., 1991, 2006, 2007).

The Eastern Kunlun Orogen (EKO) hosts abundant mafic–ultramafic complexes, containing Ni, Cu, and Co economic mineralization, and Silurian-Devonian has been

* Corresponding author. E-mail: sunfeng0669@sina.com

the most significant Ni-Cu metallogenic period, including the Shitoukengde (424 Ma; Zhou Wei et al., 2015), Binggounan, Maxingdawannan, Akechukesai, and Langmuri ore spots/deposits, particularly the recently discovered Xiariham large-scale Ni–Cu deposit (394–439 Ma; Wang Guan et al., 2014a; Jiang Changyi et al., 2015; Li et al., 2015; Peng et al., 2016; Song et al., 2016). Increased Ni–Cu exploration in the EKO, stream sediment surveys in Shitoukengde area performed by the Sichuan Bureau of Geology and Mineral Exploration in 2013, led to the discovery of Ni-Cu-hosted complexes of the Shitoukengde, with initial grades of 903 t Cu, 68,943 t Ni, and 3309 t Co recently. Drilling programs conducted during 2014–2015 intersected six Ni–Cu-bearing orebodies that have yet to be thoroughly studied (Zhou Wei et al., 2015, 2016) owing to its new discovery. Although the Silurian-Devonian Ni-Cu metallogenic events have been thoroughly studied on ore-forming time, genesis, magmatic source and evolution (Li Shijin et al., 2012; Wang Guan et al., 2014a; Jiang Changyi et al., 2015; Li et al., 2015; Zhou Wei et al., 2015, 2016; Peng et al., 2016; Song et al., 2016), there is still a debate on the geodynamic setting. Same researchers considered that Xiarihamu complexes formed in the island-arc background related to the subduction of Proto-Thetys Oceanic plate (Jiang Changyi et al., 2015; Li et al., 2015), while others suggested the post-collisional, extensional setting after Proto-Thetys Ocean closed (Li Shijin et al., 2012; Wang Guan et al., 2014a; Peng et al., 2016). This study presents the results of zircon U-Pb dating and Hf isotopes as well as whole-rock geochemical, Sr-Nd-Pb and sulfide S isotopic analyses of the Shitoukengde Ni-Cu deposit to discusses the timing of mafic-ultramafic magmatism, magmatic sources, ore genesis, tectonic setting and geodynamic process.

2 Regional Geological Setting

The Eastern Kunlun Orogen is located in the western segment of the Central Orogenic Belt in mainland China (Fig. 1a), which is bordered by the Qaidam Block (QDB) to the north and the Bayan Har-Songanganzi Terrane (BHSG) to the south. The Eastern Kunlun metallogenic belt trends E–W and is ~1500 km long and 50–200 km wide. Its northern and southern parts differ significantly in terms of basement and geological characteristics, and they are separated by the Middle Kunlun Fault. Sun Fengyue et al. (2009) considered the EKO to be a continental marginal orogen resulted from the Wanbaogou oceanic basalt plateau (OBP), as a "soft basement", collaged northward to the Qaidam Block, and records multiple stages of orogeny. Several belts are divided by the E-W-trending regional faults from north to south: the Caledonian back-arc rift belt of north Eastern Kunlun (CBNK), the basement uplifting and granite belt of middle Eastern Kunlun (BGMK), the composite collage belt of south Eastern Kunlun (CCSK), the Anyemaqen Suture Belt (ASB) and the Northern Bayan Har Orogen (NBHO) (Sun Fengyue et al., 2009; Fig. 1b). The CBNK and BGMK, located north of the Middle Kunlun Fault, have a crystalline basement composed of the Paleoproterozoic Jinshuikou Group, whereas the CCSK is a complex comprising a Meso–Neoproterozoic oceanic basalt plateau and a continental collage belt.

The Shitoukengde Ni–Cu deposit, located in the town of Zongjia, Dunlan County, Qinghai Province, China (96°07′04″–96°14′31″E, 35°54′21″–35°58′18″N), formed in the BGMK, near the Middle Kunlun Fault (Fig. 1c). The regional strata are dominated by Proterozoic, Triassic, minor Jurassic, and Tertiary sedimentary rocks (Fig. 1c), and they are mainly biotite–plagioclase gneisses, dolomite quartz schists, and diopside marbles of Paleoproterozoic Jinshuikou Group, as well as intermediate volcanics, carbonates, and sandstones of Meso-Neoproterozoic Wanbaogou Group. The widespread magmatic suite comprises Cu–Ni-bearing Silurian–Devonian mafic–ultramafic intrusions, and abundant Triassic granites. The study area is crossed by the E–W-trending North Kunlun, Middle Kunlun, and South Kunlun regional faults. In addition, several secondary NW–WNW-trending faults associated with sinistral rotation and compressive shearing have controlled the locations of Triassic hydrothermal vein deposits in the area.

3 Geological Setting of the Shitoukengde Deposit

The country rocks of Shitoukengde deposit are mainly Paleoproterozoic Jinshuikou Group and Meso–Neoproterozoic Wanbaogou Group metamorphic rocks. The Jinshuikou Group, comprising amphibole–plagioclase and biotite–plagioclase gneisses, diopside marble, and quartzite, hosts the No. I and II complexes. However, the No. III complex intrudes the Meso–Neoproterozoic Wanbaogou Group, including carbonatite with minor tuffaceous slate and limestone in the southern part of the deposit. Minor volcanic and clastic rocks of the Late Triassic Babaoshan Formation, and Quaternary sediments occur locally. The N–S-trending Haideguole–Laren and Wenlengsi–Dawaqie faults, forming part of the Middle Kunlun structure, cross-cut the Shitoukengde deposit, together with NW–SE- and NE–SW-trending secondary faults. Mineralized mafic–ultramafic intrusives of the Laren Complex and intermediate–acidic plutons are

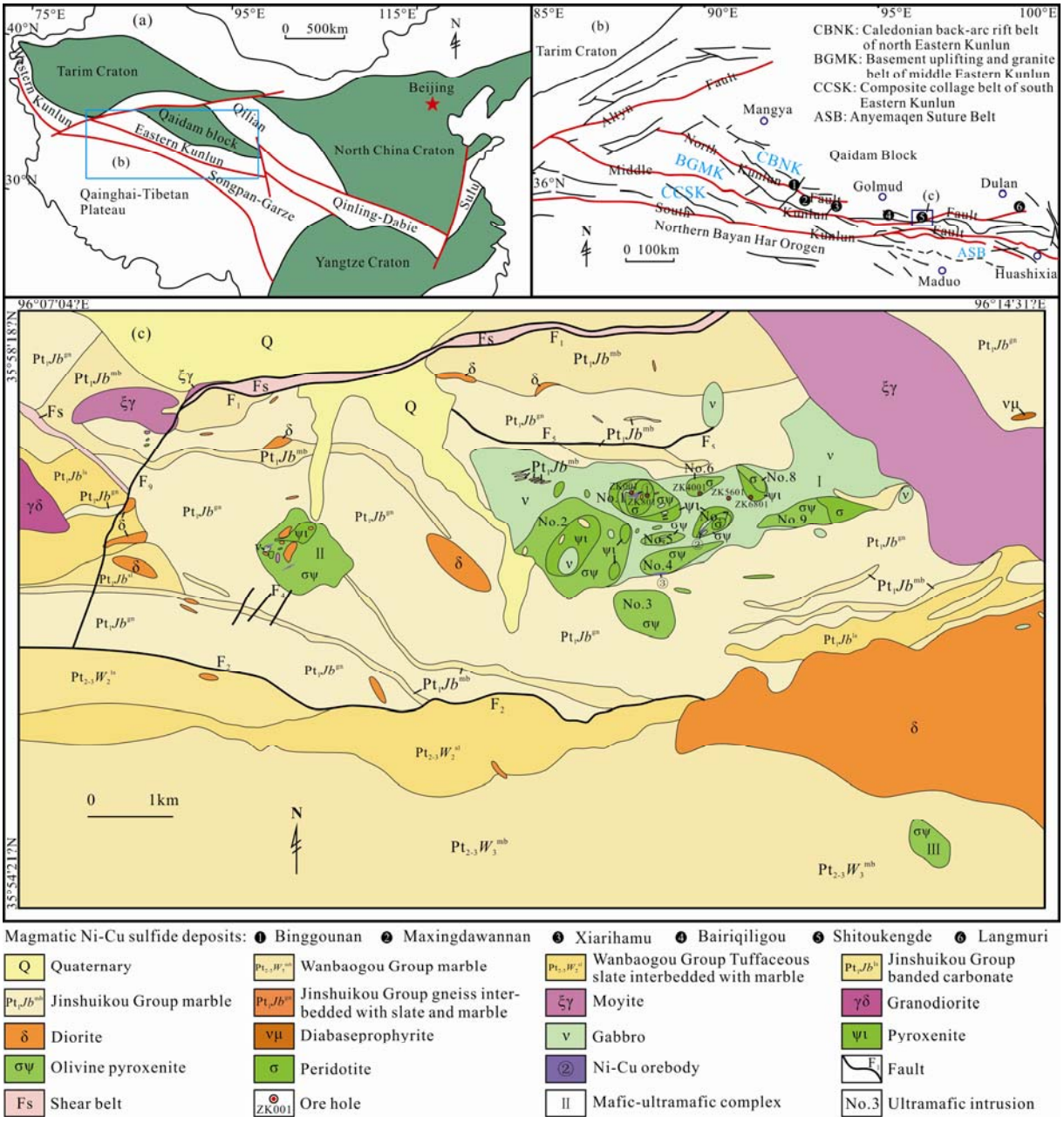

Fig. 1. Geological map showing (a, b) the regional structure of the eastern Kunlun Orogenic Belt, and (c) geology of the Shitoukengde Cu–Ni deposit (modified from Zhou et al., 2016).

oriented E–W in the study area (Fig. 1c). Meanwhile, there are some moyite, granodiorite, diorite, quartz diorite and diabase prophyrite present in the eastern of Shitoukengde (Fig. 1c).

The Shitoukengde deposit contains three mafic-ultramafic complexes that intruded the Proterozoic strata, and the No. I complex is the main host of the Ni-Cu mineralization (Fig. 1c). Economic Ni–Cu sulfide ores have also been discovered in the No. I complex, where evidence of strong mineralization has been obtained from trench and drill-core samples collected during recent prospecting work. As the two other complexes do not show any significant mineralization, so mainly complex I is discussed here. The No. I mafic-ultramafic complex, the largest complex in this deposit, is located in the northeast part of the ore district, strikes approximately E-W, and is elongate. It is 3.8–4.6 km long and 0.6–1.2 km wide with an exposed area about 5.2 km^2. A few marble xenoliths were residual in No. I complex. This complex is composed mainly of gabbro, gabbronorite, websterite, orthopyroxenite, lherzolite, peridotite, pyroxene peridotite and olivine websterite, and olivine websterite and pyroxene peridotite are the most important Ni-Cu-hosted rocks. Field relationships show that the gabbro emplaced

earliest and is most extensive, followed by the pyroxenite and peridotite. Many small ultramafic intrusions, hosted the most significant Ni-Cu mineralization, intruded the older gabbroic and metamorphic rocks (Fig. 1c). In this study, we have further subdivided the No. I complex into nine stocks, namely No. 1–No. 9 in Figure 1b.

Six Ni–Cu-bearing orebodies have been identified in the No. I complex (No. ①–⑥), of which No. ① and No. ④ are the largest). The No. ① orebody consists of medium- to coarse-grained pyroxenites and olivine websterite comprising disseminated, conglomeration and massive sulfide ores. It is 235 m long, 20–30 m wide, strikes at 075° and dips at 80° to the NW (Fig. 2). Annabergites are commonly observed on the weathered surfaces of this ore body, and assemblage of pentlandite, pyrrhotine and chalcopyrite is hosted in fresh ores. A total of 21 samples were collected and analyzed from the TC004 and TC005, averaging 1.27% Ni over 28.34 m. A total of 22 samples were collected and analyzed from BT0201, averaging 1.09% Ni over 30.81 m. Meanwhile, the No.④ ore body is concealed Ni-Cu orebody, containing medium-grained pyroxenites and medium- to fine-grained olivine pyroxenites with disseminated, conglomeration and massive sulfide ores. Boreholes ZK4001 and ZK5601 contain 0.2%–0.6% Ni over 120.75 m, and borehole ZK6801 contains 0.2%–0.41% Ni over 50.97 m (Fig. 2).

No. ② orebody: a Ni-Cu orebody, about 2.7 m wide, strikes at 10°–30° and dips at 50°–75° to the SE. Medium-grained olivine pyroxenolite is the Ni-Cu-hosted rock with the average grade of Ni 0.37%.

No. ③ orebody: a Ni-Cu orebody, about 2.0 m wide, strikes near E-W, inclination and dip are not clear. Medium-grained olivine pyroxenolite is the Ni-Cu-hosted rock with the average grade of Ni 0.22%.

No. ⑤ orebody: a concealed Ni-Cu orebody, about 4.5 m wide. Medium- to fine-grained olivine pyroxenolite is the Ni-Cu-hosted rock with the grade of Ni 0.20%–0.63%.

No. ⑥ orebody: a concealed Ni-Cu orebody, about 6.0 m wide. Medium- to fine-grained olivine pyroxenolite and peridotite are the Ni-Cu-hosted rock with the grade of Ni 0.20%–0.37%.

In general, the deposit has a weakly post-magmatic hydrothermal alteration with a few serpentines, tremolites and chlorites. Sulfides in the deposit contain the primary magmaitc sulfide, including pentlandite, pyrrhotite, chalcopyrite with minor chronmite and magnenite (Fig. 3), and hydrothermal-related sulfide, such as pyrite, violarite, and bornite. Meanwhile, many oxide minerals, such as annabergite, malachite and limonite, occur on the weathered surface. Pentlandite, pyrrhotite, and chalcopyrite are intergrown, and skeletal pentlandite grains are developed at the margins of pyrrhotite grains (Fig. 3). The sulfides are typically idiomorphic–hypidiomorphic and are not equigranular, showing

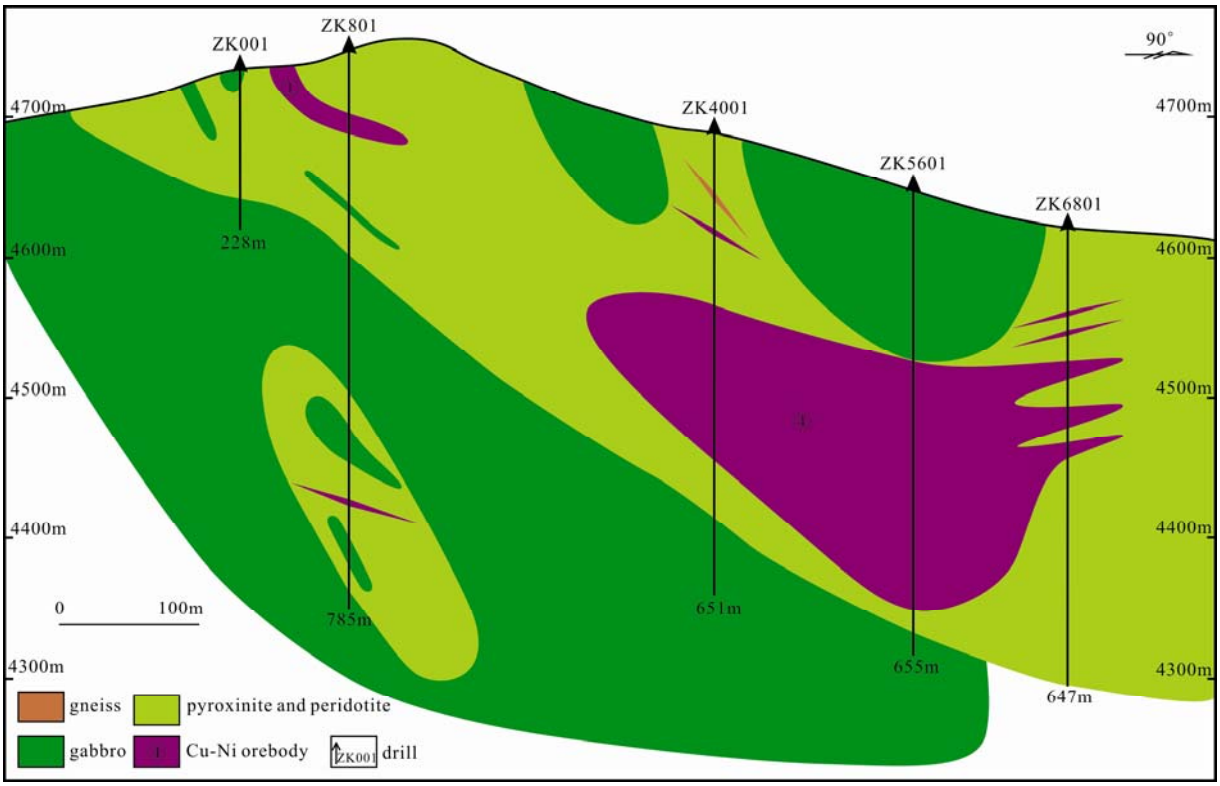

Fig. 2. Cross-section of the No. I mafic–ultramafic complex of the Shitoukengde Ni-Cu deposit showing the location and depth of boreholes ZK001, ZK801, ZK4001, ZK5601, and ZK6801.

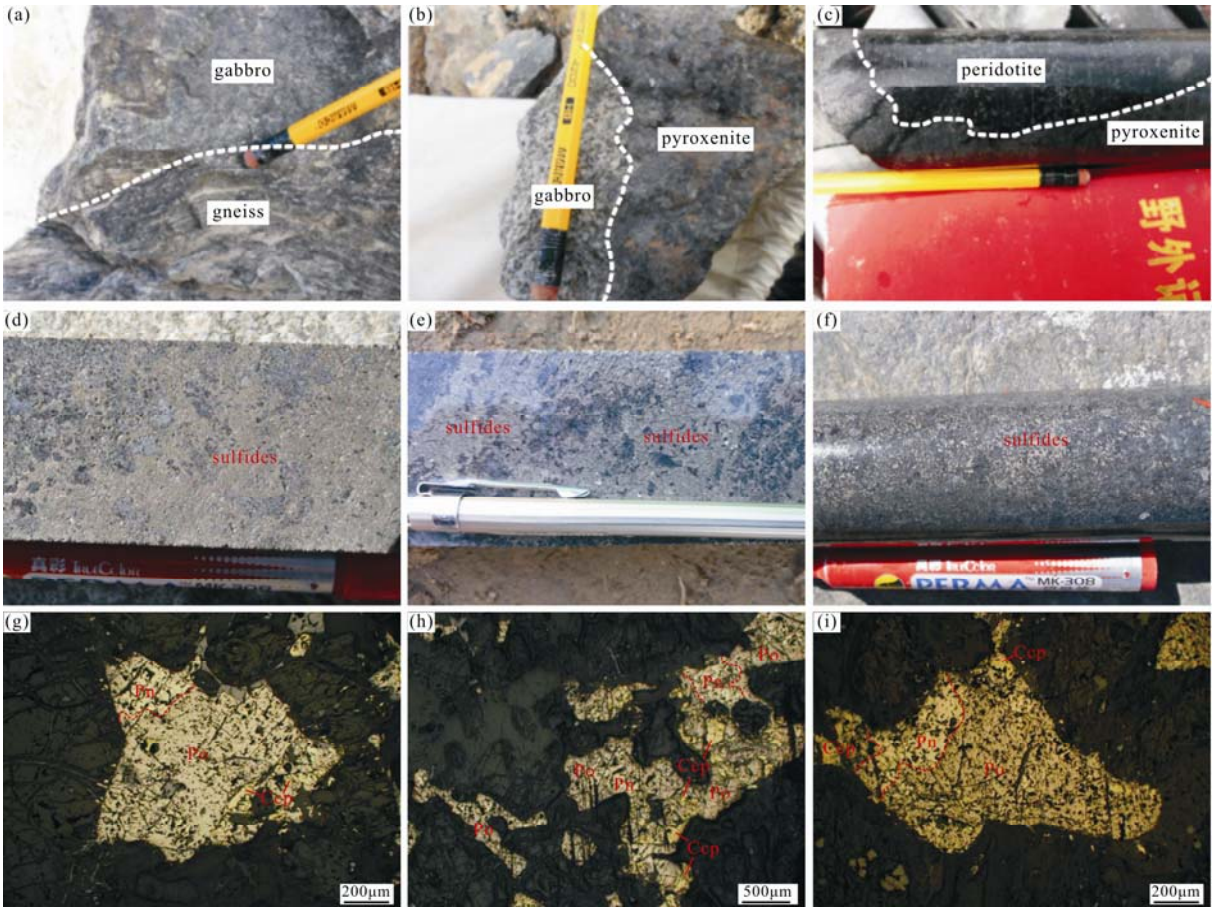

Fig. 3. Field photographs of mafic-ultramafic rocks (a, b, c), Ni-Cu ores (d, e, f) and photomicrographs of sulfides from No. Ⅰ mafic-ultramafic complex at Shitoukengde (g, h, i; plane polarized light).
(a), Gabbro intruded gneiss (after Zhou et al., 2016); (b), The sharp contact between gabbro and pyroxenite (after Zhou et al., 2016); (c), The sharp contact between peridotite and pyroxenite (after Zhou et al., 2016); (d), (e), The massive Ni-Cu ores; f-Ni-Cu ores with sideronitic texture; (g), (h), (i), Primary pentlandites, chalcopyrites and pyrrhotites in Ni-Cu ores under the microscope. Pn: pentlandite; Ccp: chalcopyrite; Po: pyrrohotite.

metasomatic and sideronitic textures (Fig. 3). The ore is disseminated, showing stellate and mottled structures.

4 Sample Descriptions and Analytical Techniques

4.1 Sample descriptions

The No. I complex of the Shitoukengde deposit was sampled due to its size, extensive mineralization, and succession of mafic–ultramafic rocks, including gabbro (Fig. 4a), olivine websterite (Fig. 4b–c), websterite (Fig. 4d), pyroxenite allivalite (Fig. 4e), orthopyroxenite (Fig. 4f), olivine pyroxenite, pyroxene peridotite, olivine gabbro, and gabbronorite. Samples of olivine websterite (14STKD-ZK001-N1) and gabbro (14STKD-ZK001-N2), were selected to analyse for zircon U-Pb geochronology and Hf isotopes, whole-rock geochemistry and Sr-Nd-Pb isotopes.

The gabbro is gray in color and composed of medium-grained idiomorphic–subhedral, is massive, and mainly contain plagioclase (~60%), orthopyroxene (~5%), clinopyroxene (~38%), olivine (~5%), and sulfides (~2%; Fig. 4a). The plagioclase grains are euhedral and clintheriform, measuring 3.5–5.0 mm in length and showing polysynthetic twinning under cross-polarized light. Pyroxenes are subhedral and 1.5–2.0 mm long.

The olivine websterite is gray–black in color, medium- to fine-grained, massive, and contains clinopyroxene (~30%), orthopyroxene (~55%), olivine (~10%), and minor sulfides (~5%; Fig. 4b–c). The pyroxenes are subhedral and weakly altered, measuring 2.0–2.5 mm. Olivine grains are subhedral, 1.5–2.0 mm in size, and have been serpentinized.

4.2 Analytical methods

4.2.1 Zircon U-Pb dating

Zircons were separated from whole-rock samples using the conventional heavy liquid and magnetic techniques, and then by handpicking under a binocular microscope, at the Langfang Regional Geological Survey, Hebei Province, China. The handpicked zircons were examined under transmitted and reflected light with an optical

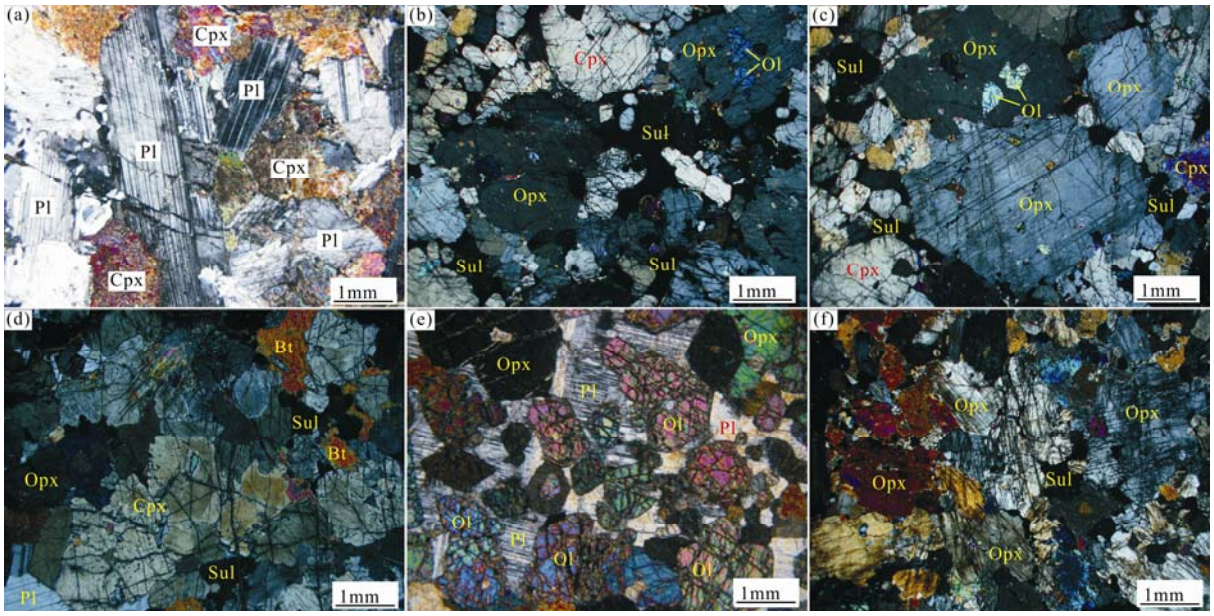

Fig. 4. Photomicrographs of ultramafic–mafic rocks of the No. I complex of the Shitoukengde deposit (crossed-polarized light).
(a), Gabbro; (b), (c), Olivine websterite; (d), Websterite; (e), Pyroxenite troctolite; (f), Orthopyroxenite. Pl: plagioclase; Cpx: clinopyroxene; Opx: orthopyroxene; Ol: olivine; Bt: biotite; Sul: sulfide.

microscope. To reveal their internal structures, cathodoluminescence (CL) images were obtained using a JEOL scanning electron microscope housed at the State Key Laboratory of Geological Processes and Mineral Resources, China University of Geosciences, Wuhan, China. The testing method, testing process and data processing are introduced in reference of Tang et al. (2015) and the data are shown in Table 1.

4.2.2 Whole-rock geochemistry analysis

For geochemical analysis, whole-rock samples, after the removal of altered surfaces, were crushed in an agate mill to ~200 mesh. X-ray fluorescence (XRF; PW1401/10) using fused-glass disks and ICP-MS (Agilent 7500a with a shield torch) were used to measure the major and trace elements compositions, respectively, at the Testing Center of Jilin University, after acid digestion of samples in Teflon bombs. The analytical results for the BHVO-1 (basalt), BCR-2 (basalt), and AGV-1 (andesite) standards indicate that the analytical precision for major elements is better than 5%, and for trace elements, generally better than 5% when the content >10ppm, and better than 10% when <10ppm. The analytical results of major and trace elements are listed in Table 2.

4.2.3 Hf isotope analysis

In situ zircon Hf isotope analyses were carried out using a NewWave UP213 laser-ablation microprobe, attached to a Neptune multi-collector ICP‐MS at the Institute of Mineral Resources, Chinese Academy of Geological Sciences. Instrumental conditions and data acquisition techniques have been comprehensively described by Wu et al. (2006). Lu-Hf isotopic measurements were made on the same zircon grains previously analyzed for U-Pb with ablation pits 55 μm in diameter, repetition rates of 8–10 Hz, laser beam energy density of 10 J/cm^2, and an ablation time of 26s. The testing method, testing process and data processing are introduced in reference of Guo et al. (2012) and the data are shown in Table 3.

4.2.4 Whole-rock Sr-Nd-Pb isotope analysis

Whole-rock Sr-Nd-Pb isotope analysis were carried out at Analytical Laboratory of the Beijing Research Institute of Uranium Geology, China, by using an ISOPROBE-T thermal ionization mass spectrometer. Sample powders were dissolved in HF + HNO_3 + $HClO_4$ mixture. Digested samples were dried and redissolved in 6 mol/L NHCl, dried again and redissolved in 0.5 mol/L NHCl (for Sr and Nd separation) or 0.5 mol/L NHBr (for Pb separation). Sr and Nd fractions were separated following standard chromatographic techniques using AG50x8 and PTFE–HDEHP resins with HCl as eluent, while Pb fraction was separated using strong alkali anion exchange resin with HBr and HCl as eluents. Measured Nd isotopic compositions were corrected for instrumental mass bias using a $^{86}Sr/^{88}Sr$ and $^{146}Nd/^{144}Nd$ values of 0.1194 and 0.7219. Analysis of the Nd standard JNdi-1 gave a $^{143}Nd/^{144}Nd$ value of 0.512109±3. For convenience, $^{143}Nd/^{144}Nd$ ratios are expressed as εNd (Jacobsen and Wasserburg, 1980). A factor of 1‰ per mass unit for

Table 1 LA-ICP-MS U-Pb zircon dating results of olivine websterite (14STKD-ZK001-N1) and gabbro (14STKD-ZK001-N2) in the No. Ⅰ mafic-ultramafic complex

Analysis spots	Pb	Th	U	Th/U	$^{207}Pb/^{206}Pb$		$^{207}Pb/^{235}U$		$^{206}Pb/^{238}U$		$^{208}Pb/^{232}Th$		$^{207}Pb/^{206}Pb$		$^{207}Pb/^{235}U$		$^{206}Pb/^{238}U$		$^{208}Pb/^{232}Th$	
	ppm	ppm	ppm		Ratio	1σ	Ratio	1σ	Ratio	1σ	Ratio	1σ	Age (Ma)	1σ	Age (Ma)	1σ	Age (Ma)	1σ	Age (Ma)	1σ
14STKD-ZK001-N1-01	1297	841	19606	0.04	0.0565	0.0008	0.5308	0.0091	0.0677	0.0006	0.0310	0.0013	472	31	432	6	422	4	616	26
14STKD-ZK001-N1-02	963	786	14156	0.06	0.0546	0.0008	0.5152	0.0081	0.0680	0.0007	0.0237	0.0005	398	33	422	5	424	4	473	9
14STKD-ZK001-N1-03	1076	1173	14246	0.08	0.0546	0.0007	0.5120	0.0068	0.0676	0.0004	0.0229	0.0003	394	34	420	5	422	3	458	7
14STKD-ZK001-N1-04	1144	758	16576	0.05	0.0576	0.0007	0.5421	0.0087	0.0678	0.0006	0.0317	0.0011	522	28	440	6	423	4	632	22
14STKD-ZK001-N1-05	1579	1815	18622	0.10	0.0558	0.0008	0.5206	0.0083	0.0676	0.0008	0.0256	0.0007	443	33	426	6	422	5	511	13
14STKD-ZK001-N1-06	996	697	14485	0.05	0.0570	0.0010	0.5328	0.0118	0.0675	0.0007	0.0299	0.0007	500	39	434	8	421	5	595	15
14STKD-ZK001-N1-07	1954	3225	23086	0.14	0.0552	0.0014	0.5168	0.0157	0.0676	0.0013	0.0190	0.0008	420	59	423	11	422	8	380	15
14STKD-ZK001-N1-08	966	1084	13086	0.08	0.0551	0.0008	0.5149	0.0081	0.0677	0.0005	0.0224	0.0004	413	33	422	5	422	3	447	8
14STKD-ZK001-N1-09	1192	878	19125	0.05	0.0560	0.0008	0.5252	0.0085	0.0676	0.0006	0.0229	0.0005	454	33	429	6	422	4	458	9
14STKD-ZK001-N1-10	1021	700	15810	0.04	0.0579	0.0008	0.5452	0.0120	0.0677	0.0010	0.0312	0.0012	524	36	442	8	422	6	621	24
14STKD-ZK001-N1-11	940	775	14201	0.05	0.0559	0.0008	0.5252	0.0085	0.0678	0.0006	0.0224	0.0006	450	33	429	6	423	3	447	12
14STKD-ZK001-N1-12	1188	939	18226	0.05	0.0561	0.0007	0.5283	0.0074	0.0679	0.0005	0.0230	0.0004	457	30	431	5	423	3	461	8
14STKD-ZK001-N1-13	950	784	14648	0.05	0.0561	0.0007	0.5261	0.0075	0.0677	0.0005	0.0229	0.0004	454	25	429	5	422	3	458	8
14STKD-ZK001-N1-14	1106	857	17890	0.05	0.0563	0.0007	0.5281	0.0081	0.0676	0.0008	0.0227	0.0004	461	32	431	5	422	5	454	9
14STKD-ZK001-N1-15	995	689	16008	0.04	0.0568	0.0008	0.5347	0.0072	0.0676	0.0005	0.0235	0.0005	487	31	435	5	422	3	469	9
14STKD-ZK001-N1-16	1071	881	15275	0.06	0.0579	0.0009	0.5434	0.0086	0.0674	0.0006	0.0273	0.0006	528	33	441	6	421	4	545	11
14STKD-ZK001-N1-17	1149	705	15834	0.04	0.0585	0.0009	0.5478	0.0115	0.0676	0.0008	0.0422	0.0018	550	31	444	8	422	5	835	34
14STKD-ZK001-N1-18	1092	1383	13987	0.10	0.0544	0.0007	0.5096	0.0069	0.0677	0.0005	0.0212	0.0003	387	23	418	5	422	3	424	7
14STKD-ZK001-N1-19	659	699	9212	0.08	0.0547	0.0008	0.5121	0.0102	0.0677	0.0010	0.0229	0.0005	398	31	420	7	422	6	458	10
14STKD-ZK001-N1-20	995	669	15694	0.04	0.0559	0.0009	0.5241	0.0092	0.0677	0.0006	0.0241	0.0007	450	37	428	6	422	3	481	13
14STKD-ZK001-N1-21	1434	1904	16195	0.12	0.0571	0.0010	0.5335	0.0107	0.0675	0.0008	0.0242	0.0005	494	39	434	7	421	5	483	11
14STKD-ZK001-N1-22	1197	1427	13454	0.11	0.0562	0.0011	0.5266	0.0101	0.0675	0.0005	0.0278	0.0011	457	44	430	7	421	3	554	21
14STKD-ZK001-N2-01	244	272	2779	0.10	0.0588	0.0016	0.5578	0.0160	0.0684	0.0009	0.0235	0.0009	561	59	450	10	426	6	470	17
14STKD-ZK001-N2-02	644	642	1666	0.39	0.0672	0.0017	1.1102	0.0287	0.1191	0.0012	0.0464	0.0010	856	54	758	14	725	7	917	20
14STKD-ZK001-N2-03	820	870	2719	0.32	0.0669	0.0018	1.1191	0.0340	0.1204	0.0019	0.0413	0.0010	835	56	763	16	733	11	818	20
14STKD-ZK001-N2-04	273	142	1423	0.10	0.0683	0.0019	1.4894	0.0424	0.1565	0.0015	0.0432	0.0017	880	58	926	17	937	9	855	33
14STKD-ZK001-N2-05	476	230	2010	0.11	0.0739	0.0020	1.6169	0.0460	0.1572	0.0017	0.0657	0.0021	1039	56	977	18	941	9	1285	39
14STKD-ZK001-N2-06	215	148	769	0.19	0.0679	0.0022	1.4888	0.0481	0.1575	0.0020	0.0489	0.0017	866	67	926	20	943	11	965	32
14STKD-ZK001-N2-07	272	210	975	0.21	0.0704	0.0019	1.5339	0.0437	0.1578	0.0023	0.0474	0.0015	939	56	944	18	944	13	937	29
14STKD-ZK001-N2-08	263	157	1197	0.13	0.0686	0.0018	1.5001	0.0400	0.1577	0.0015	0.0498	0.0019	887	54	930	16	944	8	982	37
14STKD-ZK001-N2-09	548	416	1501	0.28	0.0751	0.0020	1.6594	0.0498	0.1579	0.0024	0.0524	0.0017	1072	54	993	19	945	14	1032	32
14STKD-ZK001-N2-10	626	647	1181	0.55	0.0704	0.0019	1.5437	0.0414	0.1579	0.0017	0.0452	0.0011	939	56	948	17	945	10	893	22
14STKD-ZK001-N2-11	245	235	523	0.45	0.0684	0.0024	1.4949	0.0505	0.1579	0.0020	0.0459	0.0014	883	72	928	21	945	11	907	28
14STKD-ZK001-N2-12	463	430	957	0.45	0.0699	0.0020	1.5364	0.0451	0.1582	0.0018	0.0499	0.0012	928	54	945	18	947	10	984	24
14STKD-ZK001-N2-13	308	291	678	0.43	0.0706	0.0020	1.5479	0.0440	0.1585	0.0014	0.0474	0.0013	946	58	950	18	948	8	937	25
14STKD-ZK001-N2-14	218	224	431	0.52	0.0658	0.0029	1.4503	0.0647	0.1590	0.0032	0.0456	0.0017	1200	97	910	27	951	18	901	33
14STKD-ZK001-N2-15	585	368	989	0.37	0.0870	0.0023	2.6540	0.0702	0.2195	0.0018	0.0711	0.0017	1361	50	1316	20	1279	10	1388	32
14STKD-ZK001-N2-16	2029	1468	1671	0.88	0.0878	0.0017	2.9757	0.0643	0.2441	0.0024	0.0714	0.0015	1389	39	1401	16	1408	13	1394	28
14STKD-ZK001-N2-17	1054	700	1602	0.44	0.1013	0.0026	3.4516	0.0937	0.2444	0.0031	0.0625	0.0017	1650	152	1516	21	1410	16	1226	32
14STKD-ZK001-N2-18	672	386	727	0.53	0.0871	0.0024	2.9673	0.0899	0.2446	0.0034	0.0831	0.0021	1362	52	1399	23	1411	17	1614	40
14STKD-ZK001-N2-19	1213	773	1528	0.51	0.0900	0.0024	3.0631	0.0844	0.2449	0.0029	0.0725	0.0021	1425	52	1424	21	1412	15	1414	40
14STKD-ZK001-N2-20	581	389	446	0.87	0.0960	0.0030	3.4193	0.1070	0.2569	0.0038	0.0780	0.0024	1550	59	1509	25	1474	20	1517	45
14STKD-ZK001-N2-21	615	31	2152	0.01	0.1101	0.0027	4.8277	0.1196	0.3160	0.0031	0.0930	0.0048	1811	44	1790	21	1770	15	1797	89
14STKD-ZK001-N2-22	2681	670	6046	0.11	0.1083	0.0024	5.1279	0.1465	0.3409	0.0070	0.0972	0.0022	1772	41	1841	24	1891	33	1876	41
14STKD-ZK001-N2-23	836	284	664	0.43	0.1514	0.0037	9.4117	0.3068	0.4447	0.0090	0.1276	0.0031	2361	41	2379	30	2372	40	2427	56
14STKD-ZK001-N2-24	1794	566	1450	0.39	0.1571	0.0033	9.7702	0.2193	0.4464	0.0058	0.1213	0.0030	2424	34	2413	21	2379	26	2315	54

Table 2 Whole-rock major (wt%) and trace elements (ppm) compositions of the No. I mafic-ultramafic complex

Samples	14STKD-ZK0 01-Y1-1	14STKD-ZK0 01-Y1-2	14STKD-ZK0 01-Y1-3	14STKD-ZK0 01-Y1-4	14STKD-ZK0 01-Y1-5	14STKD-ZK0 01-Y1-6	14STKD-ZK0 01-Y1-7	14STKD-ZK0 01-Y2-1	14STKD-ZK0 01-Y2-2	14STKD-ZK0 01-Y2-3	14STKD-ZK0 01-Y2-4	14STKD-ZK0 01-Y2-5	14STKD-ZK0 01-Y2-6	14STKD-ZK0 01-Y2-7
Rocks	Olivine websterite							Gabbro						
SiO_2	42.80	37.92	38.67	36.49	40.56	37.19	36.41	51.92	51.14	52.01	51.94	50.43	52.21	52.15
TiO_2	0.18	0.24	0.20	0.19	0.21	0.42	0.20	0.29	0.31	0.42	0.31	0.29	0.31	0.29
Al_2O_3	4.09	3.20	2.77	2.24	4.28	2.10	2.31	16.92	15.79	16.81	12.56	18.52	16.82	17.00
TFe_2O_3	12.10	12.97	11.87	13.39	13.10	13.77	14.44	5.06	5.83	4.45	6.36	4.66	4.76	4.89
MnO	0.17	0.12	0.10	0.12	0.18	0.13	0.12	0.13	0.13	0.13	0.16	0.12	0.12	0.12
MgO	30.18	32.90	33.34	34.65	29.54	33.83	33.60	10.55	11.44	8.33	15.42	9.26	9.95	10.09
CaO	2.94	1.97	0.78	0.80	2.44	1.37	0.98	9.92	9.54	13.96	7.77	10.88	10.71	9.82
Na_2O	0.38	0.23	0.05	0.12	0.41	0.11	0.13	2.41	2.11	2.40	1.57	2.71	2.46	2.56
K_2O	0.62	0.29	0.64	0.12	0.46	0.18	0.16	0.86	1.39	0.42	1.47	0.45	0.54	0.87
P_2O_5	0.03	0.04	0.03	0.03	0.03	0.05	0.03	0.02	0.03	0.03	0.01	0.02	0.02	0.02
LOI	6.06	9.95	11.21	11.60	8.61	10.66	11.14	1.66	2.07	0.94	2.24	2.23	1.71	1.81
Total	99.54	99.83	99.64	99.74	99.80	99.82	99.53	99.76	99.79	99.90	99.81	99.56	99.62	99.63
K_2O+Na_2O	0.58	0.77	0.26	0.32	0.33	1.07	0.95	3.33	3.58	2.85	3.11	3.24	3.07	3.50
$Mg^{\#}$	83	85	84	83	82	83	82	81	80	79	83	80	81	80
m/f	4.97	5.51	5.08	4.82	4.57	4.87	4.40	4.02	3.79	3.59	4.67	3.83	4.02	3.98
La	1.96	1.17	1.52	2.54	1.56	2.38	2.23	2.61	3.19	4.47	2.01	2.81	2.63	3.26
Ce	4.29	2.53	3.11	5.99	3.13	4.59	4.42	5.43	5.86	10.16	4.47	5.83	5.46	6.38
Pr	0.85	0.59	0.67	1.10	0.67	0.80	0.81	0.99	0.99	1.61	0.91	1.02	1.00	1.06
Nd	2.69	1.63	1.91	4.02	1.89	2.32	2.46	3.25	3.28	6.39	3.20	3.46	3.46	3.50
Sm	0.96	0.72	0.74	1.35	0.76	0.87	0.91	1.14	1.10	2.00	1.22	1.17	1.22	1.16
Eu	0.51	0.42	0.44	0.54	0.45	0.48	0.49	0.78	0.73	0.98	0.73	0.87	0.79	0.81
Gd	0.87	0.52	0.55	1.29	0.54	0.67	0.76	1.12	1.11	2.13	1.24	1.14	1.26	1.13
Tb	0.15	0.12	0.11	0.22	0.11	0.13	0.14	0.22	0.23	0.40	0.24	0.19	0.21	0.18
Dy	0.89	0.58	0.60	1.32	0.55	0.72	0.83	1.21	1.23	2.24	1.39	1.24	1.36	1.22
Ho	0.19	0.13	0.13	0.26	0.13	0.16	0.18	0.27	0.27	0.48	0.30	0.24	0.28	0.23
Er	0.53	0.39	0.37	0.78	0.35	0.47	0.51	0.73	0.73	1.30	0.86	0.74	0.81	0.70
Tm	0.08	0.06	0.06	0.11	0.06	0.07	0.08	0.11	0.10	0.17	0.12	0.10	0.11	0.10
Yb	0.48	0.37	0.36	0.69	0.35	0.44	0.49	0.69	0.65	1.09	0.77	0.70	0.72	0.68
Lu	0.07	0.06	0.06	0.09	0.05	0.06	0.07	0.10	0.10	0.18	0.12	0.09	0.10	0.10
∑REE	14.5	9.29	10.6	20.3	10.6	14.2	14.4	18.7	19.6	33.6	17.6	19.6	19.4	20.5
LREE	11.3	7.07	8.39	15.5	8.47	11.4	11.3	14.2	15.1	25.6	12.5	15.2	14.6	16.2
$(La/Yb)_N$	2.93	2.25	3.05	2.63	3.20	3.88	3.26	2.73	3.53	2.96	1.88	2.88	2.61	3.42
$(La/Sm)_N$	1.32	1.05	1.32	1.21	1.33	1.77	1.59	1.48	1.88	1.44	1.07	1.55	1.39	1.82
$(Gd/Yb)_N$	1.50	1.15	1.27	1.53	1.26	1.26	1.29	1.35	1.42	1.62	1.33	1.34	1.44	1.36
Eu/Eu*	1.72	2.09	2.13	1.24	2.17	1.91	1.78	2.12	2.02	1.46	1.82	2.29	1.95	2.18
Li	4.06	3.03	2.25	2.21	2.16	6.62	6.91	7.45	11.2	3.92	10.1	9.84	5.75	7.69
Sc	10.1	7.42	8.26	12.9	8.00	12.8	11.3	19.5	20.7	22.8	23.7	18.7	22.3	18.4
V	43.1	17.4	19.5	50.9	22.1	52.8	47.1	126	131	152	139	129	147	126
Cr	2619	3021	1707	3222	1929	1401	1993	410	546	601	1655	436	490	398
Co	162	174	167	177	167	146	152	43.4	46.8	36	71.2	41.6	40.7	41.7
Ni	960	1406	1167	1077	1167	1103	1124	45.5	91.1	57.6	265	40.8	36.8	45.8
Cu	329	201	120	317	109	132	231	23.4	44.5	46.7	29.6	48.9	32.5	26.6
Zn	86.2	107	86.4	91.6	91.7	80.0	82.6	33.2	35.8	28.1	50.9	36.4	29.3	30.8
Ga	4.63	5.44	3.34	4.52	3.65	5.09	5.60	13.2	12.5	13.8	10.8	14.5	13.0	13.4
Ge	3.24	3.40	3.58	3.79	3.51	3.53	3.34	2.33	2.47	2.33	2.75	2.15	2.34	2.23
Rb	13.1	34.1	7.09	8.76	7.42	28.0	19.9	37.4	60.6	15.4	68.3	19.4	24.3	36.6
Sr	39.7	14.8	25.4	17.7	26.4	60.8	60.3	393	355	443	255	419	570	400
Y	4.05	3.39	3.15	6.40	3.03	3.55	4.30	5.61	5.57	9.56	6.40	5.53	6.13	5.73
Zr	15.4	8.77	11.0	25.4	12.3	17.9	16.8	12.8	17.0	25.5	12.3	16.4	17.3	16.4
Nb	0.86	1.65	0.73	1.24	0.72	1.64	1.42	0.88	0.74	1.48	1.02	0.79	0.79	1.24
Ba	27.4	59.3	14.7	21.6	16.9	48.6	55.9	110	234	78.1	153	77.7	89.4	104
Hf	0.89	0.62	0.70	1.12	0.71	1.06	0.89	0.87	0.93	1.35	0.90	0.93	1.00	0.91
Ta	0.17	0.24	0.36	0.45	0.36	0.61	0.23	0.23	0.23	0.26	0.30	0.31	0.26	0.31
Pb	4.60	3.36	2.14	3.46	2.39	6.14	3.34	8.61	6.57	7.35	4.86	9.51	6.34	11.5
Bi	0.78	0.71	0.48	0.72	0.48	0.78	0.57	0.42	0.44	0.49	0.51	0.42	0.42	0.45
Th	1.65	1.24	1.43	1.84	1.49	2.23	1.55	1.80	1.65	3.47	1.48	1.76	1.71	1.80
U	0.18	0.03	0.03	0.14	0.03	0.43	0.03	0.04	0.05	0.62	0.30	0.02	0.03	0.11

Table 3 Zircon Lu-Hf isotopic compositions of olivine websterite in the No. I mafic-ultramafic complex

Sample	t(Ma)	$^{176}Yb/^{177}Hf$	2σ	$^{176}Lu/^{177}Hf$	2σ	$^{176}Hf/^{177}Hf$	2σ	$\varepsilon_{Hf}(0)$	$\varepsilon_{Hf}(t)$	2σ	T_{DM1}	T_{DM2}	$f_{Lu/Hf}$
14STKD-ZK001-N1-01	422	0.048031	0.000781	0.001500	0.000036	0.282256	0.000019	−18.2	−9.4	0.7	1424	1999	−0.95
14STKD-ZK001-N1-02	424	0.013577	0.000206	0.000480	0.000003	0.282364	0.000017	−14.4	−5.2	0.6	1237	1740	−0.99
14STKD-ZK001-N1-03	422	0.015653	0.000204	0.000558	0.000006	0.282356	0.000017	−14.7	−5.6	0.6	1250	1759	−0.98
14STKD-ZK001-N1-04	423	0.012135	0.000228	0.000427	0.000004	0.282397	0.000014	−13.3	−4.1	0.5	1190	1666	−0.99
14STKD-ZK001-N1-05	422	0.038116	0.000607	0.001297	0.000021	0.282367	0.000017	−14.3	−5.4	0.6	1260	1748	−0.96
14STKD-ZK001-N1-06	421	0.042006	0.001068	0.001393	0.000027	0.282316	0.000028	−16.1	−7.3	1.0	1335	1864	−0.96
14STKD-ZK001-N1-07	422	0.016699	0.000198	0.000614	0.000004	0.282411	0.000016	−12.8	−3.7	0.6	1177	1639	−0.98
14STKD-ZK001-N1-08	422	0.016749	0.000240	0.000607	0.000005	0.282322	0.000017	−15.9	−6.8	0.6	1300	1837	−0.98
14STKD-ZK001-N1-09	422	0.030016	0.000579	0.000987	0.000022	0.282684	0.000030	−3.1	5.9	1.1	804	1031	−0.97
14STKD-ZK001-N1-10	422	0.015420	0.000101	0.000522	0.000001	0.282305	0.000021	−16.5	−7.4	0.7	1320	1873	−0.98
14STKD-ZK001-N1-11	423	0.030995	0.000213	0.001037	0.000017	0.282374	0.000020	−14.1	−5.0	0.7	1241	1727	−0.97
14STKD-ZK001-N1-12	423	0.015620	0.000177	0.000567	0.000004	0.282381	0.000015	−13.8	−4.7	0.5	1216	1704	−0.98
14STKD-ZK001-N1-13	422	0.013280	0.000113	0.000467	0.000006	0.282394	0.000014	−13.4	−4.2	0.5	1195	1674	−0.99
14STKD-ZK001-N1-14	422	0.020707	0.001315	0.000693	0.000035	0.282353	0.000019	−14.8	−5.7	0.7	1259	1768	−0.98
14STKD-ZK001-N1-15	422	0.030700	0.000610	0.001021	0.000019	0.282332	0.000021	−15.6	−6.6	0.7	1300	1822	−0.97
14STKD-ZK001-N1-16	421	0.011849	0.000089	0.000424	0.000004	0.282417	0.000014	−12.6	−3.4	0.5	1162	1622	−0.99

instrumental mass fractionation was applied to the Pb analyses, using NBS 981 as reference material. Measurement of the common-lead standard NBS 981 gave average values of $^{208}Pb/^{206}Pb = 2.164940 \pm 15$, $^{207}Pb/^{206}Pb = 0.914338 \pm 7$ and $^{204}Pb/^{206}Pb = 0.0591107 \pm 2$, with uncertainties of <0.1% at the 95% confidence level.

5 Results

5.1 LA-ICP-MS U–Pb zircon dating

Zircons from the olivine websterite sample (14STKD-ZK001-N1) are 80–120 μm long, charcoal, mostly wide stubby columnar, and show no oscillatory zoning (Fig. 5). The internal parts of the grains are texturally homogeneous, and there is no inherited cores (Fig. 5) and yielding Th/U values of 0.04–0.14 (Table 1), indicative of a basic magmatic origin. The U–Pb ages of 22 zircons are concordant, ranging from 421 ± 3 Ma to 424 ± 4 Ma with a weighted mean age of 422.1 ± 1.5 Ma (MSWD = 0.04; Fig. 6a), representing the timing of mineralization in the deposit.

Zircons separated from the gabbro sample (14STKD-

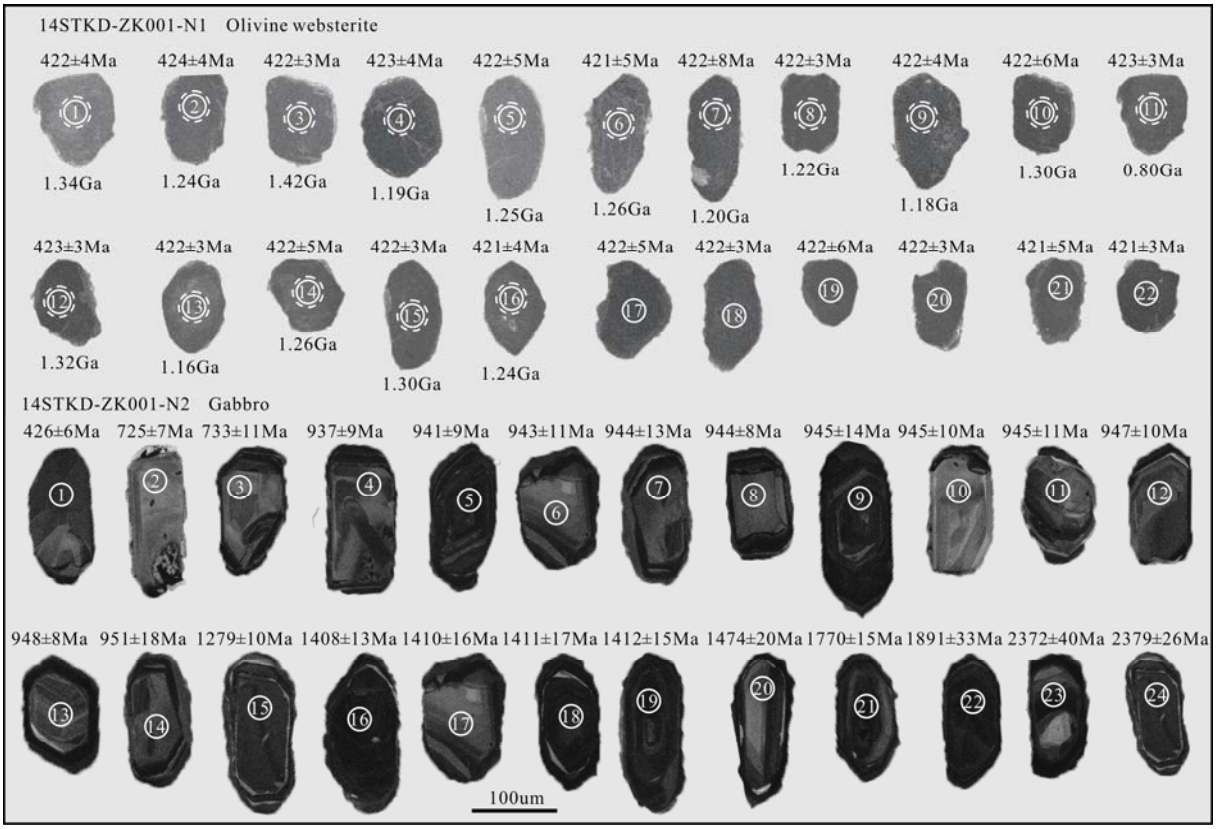

Fig. 5. Cathodoluminescence (CL) images of representative zircons of mafic-ultramafic rocks in the No. I complex selected for U-Pb isotopic analysis.

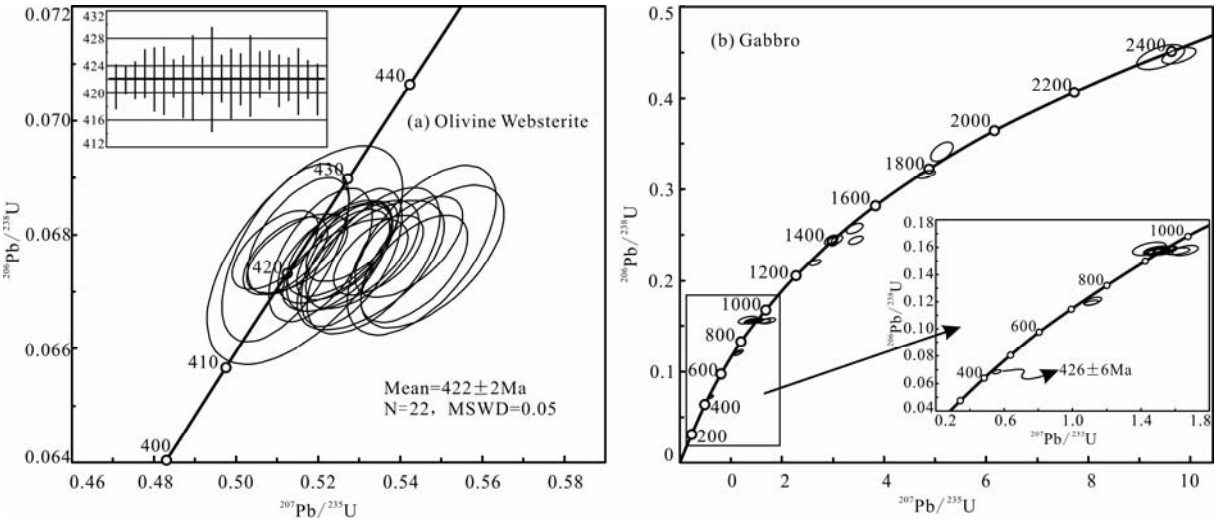

Fig. 6. U–Pb isotope concordia diagrams for analyzed zircons from (a) olivine websterite (insets show weighted mean age diagrams) and (b) gabbro.

Table 4 Whole-rock Sr-Nd isotopic compositions of the No. I mafic-ultramafic complex

Samples	Rocks	T (Ma)	Rb (ppm)	Sr (ppm)	$^{87}Rb/^{86}Sr$	$^{87}Sr/^{86}Sr$	2s	$(^{87}Sr/^{86}Sr)_i$	$\varepsilon_{Sr}(t)$	Sm (ppm)	Nd (ppm)	$^{147}Sm/^{144}Nd$	$^{143}Nd/^{144}Nd$	2s	$(^{143}Nd/^{144}Nd)_i$	$\varepsilon_{Nd}(t)$
14STKD-ZK001-B1	Olivine websterite	422	13.1	39.7	0.955822	0.719708	0.000020	0.713960	141.4	0.96	2.69	0.215730	0.512182	0.000008	0.511586	−9.93
14STKD-ZK001-B2	Olivine websterite	422	7.09	25.4	0.808069	0.713567	0.000009	0.708710	66.9	0.74	1.91	0.234213	0.512374	0.000009	0.511727	−7.17
14STKD-ZK001-B3	Gabbro	426	37.4	393	0.275565	0.716145	0.000013	0.714470	148.8	1.14	3.25	0.212038	0.512180	0.000010	0.511589	−9.77
14STKD-ZK001-B4	Gabbro	426	60.6	355	0.494535	0.721042	0.000012	0.718040	199.5	1.10	3.28	0.202733	0.512311	0.000010	0.511745	−6.72
14STKD-ZK001-B5	Gabbro	426	15.4	443	0.100649	0.714896	0.000013	0.714290	146.2	2.00	6.39	0.189204	0.512268	0.000008	0.511740	−6.82

Table 5 Whole-rock Pb isotopic compositions of the No. I mafic-ultramafic complex

Samples	Rocks	T (Ma)	U (ppm)	Th (ppm)	Pb (ppm)	$^{206}Pb/^{204}Pb$	2s	$^{207}Pb/^{204}Pb$	2s	$^{208}Pb/^{204}Pb$	2s	$(^{206}Pb/^{204}Pb)_i$	$(^{207}Pb/^{204}Pb)_i$	$(^{208}Pb/^{204}Pb)_i$
14STKD-ZK001-B1	Olivine websterite	0.18	1.65	4.60	422	18.342	0.003	15.625	0.003	38.303	0.007	18.174	15.616	37.808
14STKD-ZK001-B2	Olivine websterite	0.03	1.43	2.14	422	18.342	0.005	15.613	0.004	38.195	0.010	18.282	15.610	37.274
14STKD-ZK001-B3	Gabbro	0.04	1.80	8.61	426	18.226	0.003	15.607	0.002	38.169	0.007	18.206	15.606	37.879
14STKD-ZK001-B4	Gabbro	0.05	1.65	6.57	426	18.541	0.004	15.633	0.003	38.639	0.010	18.508	15.631	38.286
14STKD-ZK001-B5	Gabbro	0.62	3.47	7.35	426	18.435	0.003	15.404	0.003	38.463	0.006	18.070	15.384	37.805

Table 6 S isotopic compositions of sulfides from Shitoukengde Ni-Cu deposit

Samples	Rocks	Tested minerals	$\delta^{34}S$ (‰)	References
STKD2015-II-TC01-B1	Gabbro-type disseminated ore	Pyrrhotine	3.1	This paper
STKD2015-II-TC01-S2	Gabbro-type disseminated ore	Pyrrhotine	3.2	
STKD2015-TC005-B1	Pyroxenite-type disseminated ore	Pyrrhotine	2.6	
STKD2015-TC005-S1	Pyroxenite-type disseminated ore	Pyrrhotine	2.6	
S-22	Gabbro-type disseminated ore	-	2.1	Zhou, 2016
S-33	Gabbro-type disseminated ore	-	1.9	
002-6	Pyroxenite-type disseminated ore	-	2.3	
002-8	Pyroxenite-type disseminated ore	-	2.5	
S-18	Peridotite-type disseminated ore	-	3.2	
4001-5	Peridotite-type disseminated ore	-	4.3	
4001-6	Peridotite-type disseminated ore	-	3.8	

ZK001-N2) are 100–150 μm long, stubby columnar (Fig. 5), show obvious oscillatory zoning and rhythmically zoned textures (except the first zircon), which are different to the zircons from basic intrusions. Only one crystallization age of 426±6 Ma was obtained from this sample, representing the crystallization age of gabbro (Fig. 6b). However, inherited zircons from this sample yield values concentrate at 940–950 Ma (Fig. 6b), in response to the Neoproterozoic magmatic event (Jin Lijie et al., 2015; Wang Guan et al., 2016).

Thus, we suggest that Shitoukengde Ni-Cu sulfide deposit formed in late Silurian (426–422 Ma), which was supported by the gabbro U-Pb age of 424 Ma (Zhou Wei et al., 2015), and they are the same to other magmatic Ni-

Cu sulfide deposits, such as Xiarihamu (394–439 Ma; Li Shijin et al., 2012; Wang Guan et al., 2014a; Jiang Changyi et al., 2015; Li et al., 2015; Peng et al., 2016; Song et al., 2016).

5.2 Geochemical characteristics

5.2.1 Major elements

The olivine websterites contain 36.41–42.80wt% SiO_2 (averaging 38.58wt %), 11.87–14.44wt % TFe_2O_3 (averaging 13.09wt%), 0.78–2.94wt% CaO (averaging 1.61wt%), 29.54–34.65wt% MgO (averaging 32.58wt%), and Na_2O+K_2O contents of 0.23–1.00wt% (averaging 0.55 wt%). These samples have $Mg^{\#}$ = 82–85 {$Mg^{\#}$ = $100\times Mg^{2+}/(Mg^{2+}+TFe^{2+})$} and m/f values {m/f = $Mg^{2+}/(TFe^{2+}+Mn^{2+})$} of 4.40–5.51.

The gabbros contain 50.43–52.21wt% SiO_2 (averaging 51.69wt%), 4.45–6.36wt% TFe_2O_3 (averaging 5.14wt%), 7.77–13.96wt% CaO (averaging 10.72wt%), 8.33–15.42 wt% MgO (averaging 10.72wt%), and Na_2O+K_2O contents of 2.82–3.50wt% (averaging 3.17wt%). They have $Mg^{\#}$ = 79–83 and m/f values of 3.59–4.67.

The rocks of complex No. I are low in SiO_2, TiO_2, and ($Na_2O + K_2O$), and high in MgO and $Mg^{\#}$. They have m/f values of 3.59–5.51 (averaging 4.44), suggests that the mafic–ultramafic complex makes it a potential source of Cu–Ni mineralization (Wu Liren, 1963). The olivine websterite spot in the ultramafic cumulate (Fig. 7a) and Tholeiitic series (Fig. 7b), while the gabbros belong to the calc-alkaline series (Fig. 7).

5.2.2 Trace elements

The ultramafic–mafic rocks in the No. I complex contain low total rare-earth-element contents (SREE = 9.29–33.60 ppm). These samples show the flat, overall similar normalized trace element patterns, and they are slightly enriched in light rare earth element (LREE) and depleted in heavy rare earth element (HREE) (Fig. 8a), with $(La/Yb)_N$, $(La/Sm)_N$, and $(Gd/Yb)_N$ values of 1.88–3.88, 1.07–1.88, and 1.15–1.62, respectively. These results indicate enrichment in light rare earth elements relative to the middle and heavy rare earth elements but only very weak fractionation of the middle and heavy rare earth elements (Fig. 8a). In addition, these rocks are characterized by the positive Eu anomalies (Eu/Eu^{*} = 1.24 –2.29).

On the primitive-mantle-normalized spidergrams (Fig.

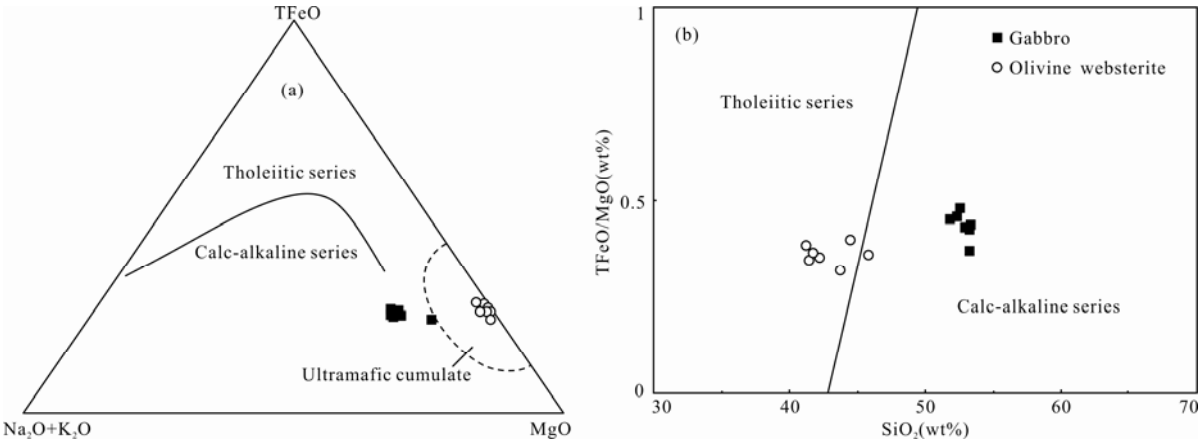

Fig. 7. TFeO-(Na_2O+K_2O)-MgO and SiO_2 vs. TFeO/MgO diagrams of the mafic-ultramafic rocks in No. I complex.

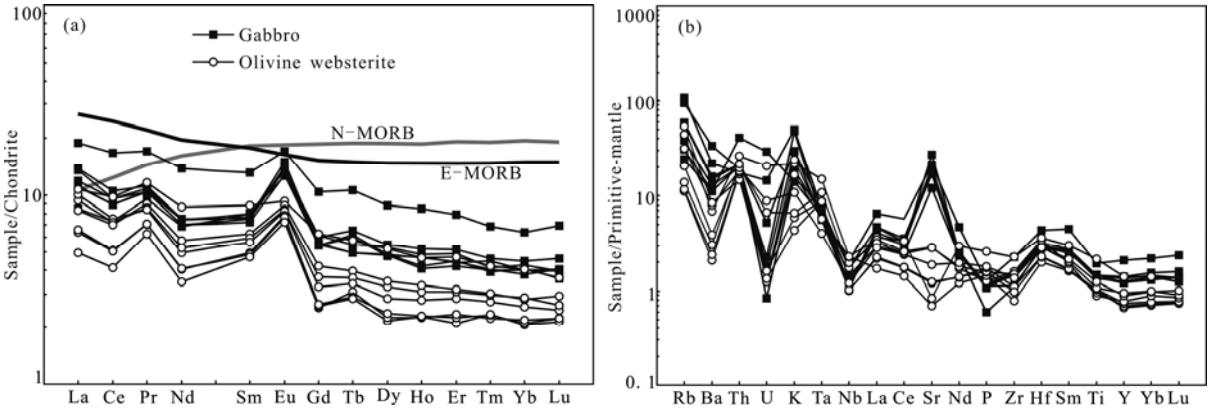

Fig. 8. Trace element characteristics of ultramafic–mafic rocks of the No. I complex showing (a) chondrite-normalized REE patterns, and (b) primitive-mantle-normalized trace element abundances.

8b), the trace element abundances of these samples are similar, and they are relatively enriched in large ion lithophile elements (LILE; e.g., K, Rb, Th) and depleted in high field strength elements (HFSE; e.g., Nb, Ta, Zr, Ti).

5.3 Hf isotopes of zircon

16 zircons of olivine websterite in No. I mafic-ultramafic complex have $^{176}Hf/^{177}Hf$ ratios between 0.282256 and 0.282684, and in response to $\varepsilon_{Hf}(t)$ values of -9.4 to 5.9 , and their T_{DM1} ages fall between 0.80 Ga and 1.42 Ga (Table 2; Fig. 9). The crystallization ages of mafic -ultramafic rocks would be approximative to the T_{DM1} ages of zircons, if their primary magmas were derived from uncontaminative depleted mantle (Wu Fuyuan et al., 2007). However, the T_{DM1} ages of olivine websterite were beyond the crystallization age (zircon U-Pb age 422 Ma), suggesting they deriving from the enriched lithospheric mantle or contamination of the crust material in the magmatic source (Wu Fuyuan et al., 2007).

5.4 Whole-rock Sr-Nd-Pb isotopes

The olivine websterite and gabbro samples in this paper have the similar Sr and Nd isotopic compositions {$\varepsilon_{Nd}(t)$= −9.93–−6.72, $(^{87}Sr/^{86}Sr)_I$ = 0.708710–0.718040} suggesting the same magmatic source. These rocks have small negative $\varepsilon_{Nd}(t)$ values and $(^{87}Sr/^{86}Sr)_i$ values that are higher than those of MORB (Sauders et al., 1988) with the characteristics of enriched mantle source. They are dispersed and all plot between the DMM (depleted MORB mantle) and EMII (II-type enriched mantle) in the diagram of $\varepsilon_{Nd}(t)$ vs. $(^{87}Sr/^{86}Sr)_i$ (Fig. 10a), approaching to Xiarihamu Sr-Nd isotopics (Peng et al., 2016), which show the evidence for evolution to an EMII end-member composition (Yang Xin et al., 2016).

The mafic-ultramafic rocks in the No. I complex have the $(^{206}Pb/^{204}Pb)_i$=18.176–18.508, $(^{207}Pb/^{204}Pb)_I$ = 15.384–15.631, and $(^{208}Pb/^{204}Pb)_I$ = 37.281–38.290. These samples plot in close to EMII on the diagrams of $(^{206}Pb/^{204}Pb)_i$ vs. $\varepsilon_{Nd}(t)$ and $(^{207}Pb/^{204}Pb)_i$ (Fig. 10b–c) and they mainly fall in MORB on the diagram of $(^{206}Pb/^{204}Pb)_i$ vs. $(^{208}Pb/^{204}Pb)_i$ (Fig. 10d), which indicates that their were probably derived from enriched mantle or contaminated greatly by the enriched component.

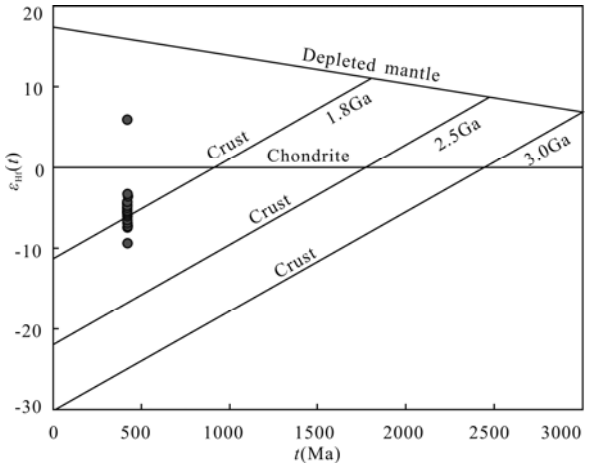

Fig. 9. Zircon Hf isotopic compositions of olivine websterite in the No. I mafic–ultramafic complex.

6 Discussion

6.1 Magmatic sources

The similar major and trace element characteristics, and Sr, Nd and Pb isotopes of the mafic-ultramafic rocks in No. I complex suggest that they were originated from a common source. Meanwhile, these rocks show the flat and similar chondrite-normalized REE patterns, and the olivine websterites contain the low SiO_2 (36.41–42.80 %), CaO (0.78–2.94 %), Na_2O (0.05–0.41 %), K_2O (0.12–0.64 %) and TiO_2 (0.18–0.42 %) concentrations, and the low SLREE (7.07–15.5 ppm), indicate that their primary magmas were derived from partial melting of depleted mantle and less possibly the enriched mantle (Fig. 8a; Sun and McDonough, 1989; Huang Qiangtai et al., 2015). What is more, this also supported by the positive $\varepsilon_{Hf}(t)$ value ($\varepsilon_{Hf}(t)$=5.9) of olivine websterite zircons. The Hf model ages of zircons may reflect the time at which they separated from depleted mantle, if the parental magma of the zircons came directly from unmodified depleted mantle. In such a case, the crystallization ages of the zircons should be roughly the same as the Hf model ages of the zircons (Wu Fuyuan et al., 2007). Thus, the zircons of olivine websterite at Shitoukengde have Hf model ages (T_{DM1} = 0.80–1.42 Ga) that are considerably older than their crystallization ages (426–422 Ma) implies that their magmatic source had been contaminated greatly by the enriched component.

It is inevitable that mantle-derived magma will experience assimilation-contamination during ascent (Peng et al., 2016) for the continental mafic-ultramafic complexes. One of the most significant evidences of this for the No. I complex is the numerous xenoliths of Paleoproterozoic Jinshuikou Group gneiss (Fig. 3a). Meanwhile, a great number of Precambrian captured zircons with the U-Pb ages peak of 940–950 Ma were obtained from the gabbros (Fig. 6a). The mafic-ultramafic rocks display the different chondrite-normalized REE patterns to those of N-MORB sourced from asthenospheric mantle (Fig. 8a) and are characterized by the enrichment in LREE and LILE (e.g., K, Rb, Th), and depletion in HREE and HFSE (e.g., Nb, Ta, P, Ti), and the gabbros have Sr of 255–570 ppm, indicate that their primary magmags had experienced some enrichment.

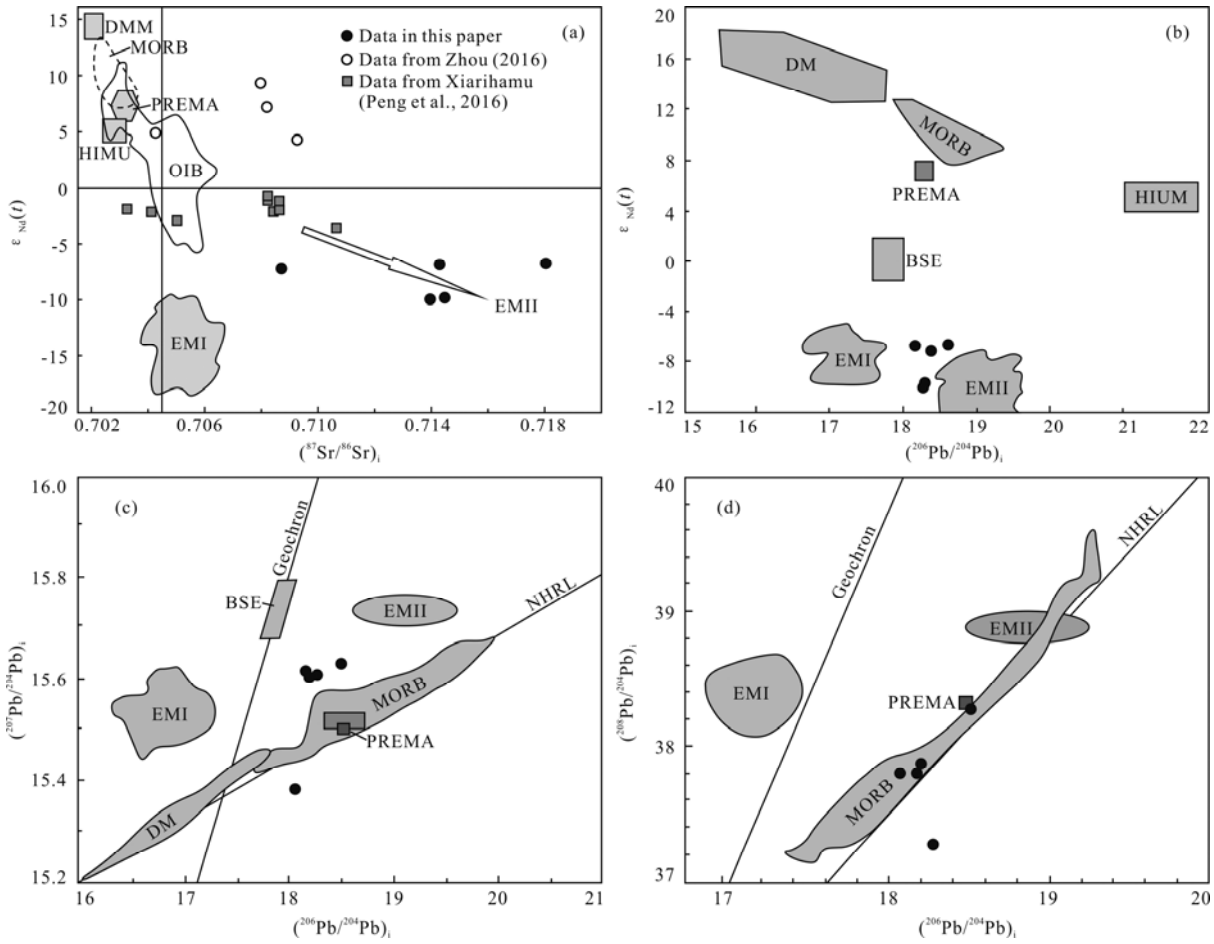

Fig. 10. Diagrams of $(^{87}Sr/^{86}Sr)_i$ vs. $\varepsilon_{Nd}(t)$, $(^{206}Pb/^{204}Pb)_i$ vs. $\varepsilon_{Nd}(t)$, $(^{206}Pb/^{204}Pb)_i$ vs. $(^{207}Pb/^{204}Pb)_i$ and $(^{206}Pb/^{204}Pb)_i$ vs. $(^{208}Pb/^{204}Pb)_i$ of the mafic–ultramafic rocks in the No. I complex.

These samples show a trend toward the EMII end member, which are similar to the Xiarihamu (Peng et al., 2016), and form an array between the DMM and EMII end members (Fig. 10). The EMI end member appears to be less possibly because they plot in the right of Geochron (Fig. 10c–d) for the EMI mantle enriching non-radioactive Sr, Nd and Pb isotopes and originating from lithospheric mantle under the continents (Hart, 1988; Menzies, 1989; Xia Zhaode et al., 2017). Therefore, we suggest that the primary magma of the Shitoukengde No. I mafic-ultramafic complex originated from asthenospheric mantle that experienced contamination of EMII component during ascent.

Crustal contamination and hybridization typically causes an elevated SiO_2, K_2O, Rb, Ba, Th, Zr, Hf, Ta/Nb, Zr/Hf, $^{87}Sr/^{86}Sr$, and $^{207}Pb/^{204}Pb$ (Zhao et al., 2007; Mir et al., 2011), a decrease in P_2O_5, TiO_2, Ti/Yb, Ce/Pb, and $^{143}Nd/^{144}Nd$ (Barker et al., 1997; Macdonald et al., 2001; Wang Guan et al., 2014a), and triggers the saturation of S in the magma (Zhang et al., 2009b). Thus, it can be identified by the covariant relationships between ratios of elements with similar distribution coefficients that are not affected by fractional crystallization or the degree of partial melting (Mecdonald et al., 2001; Jiao Jiangang et al., 2012; Wang Guan et al., 2014a; Qian Xin et al., 2016), such as Ce/Yb, La/Yb, Th/Yb, Zr/Yb, Nb/Ta and Zr/Nb. The mafic-ultramafic rocks in No. I complex show positive correlations for Ce/Yb vs. La/Yb and Th/Yb vs. Zr/Yb (Fig. 11a–b). Meanwhile, diagram of $(Th/Nb)_N$ vs. $(Sm/Yb)_N$ (Fig. 11c) shows the crustal contamination trend for these samples as well (Qian Xin et al., 2016). Furthermore, the Ti/Cr ratios of Shitoukengde No. I complex (0.45–4.42, averaging 2.18) are greater than those of the mantle (0.32; Taylor et al., 1985), whereas the continental crust is 29.19 (Taylor et al., 1985), and their Ce/Pb ratios (0.55–1.75, averaging 1.01) are smaller then those of the continental crust (<15; Furman et al., 2004) and the mantle (25 ± 5; Furman et al., 2004), suggesting the significant crustal contamination. These samples plot near the average values of the middle crust on the diagram of $(Th/Yb)_N$ vs. $(Ta/Th)_N$ (Fig. 12a) and plot between the average values of the lower and upper crust on the diagram of $(La/Nb)_N$ vs. $(Th/Ta)_N$ (Fig. 12b), which suggests that the materials responsible for contamination

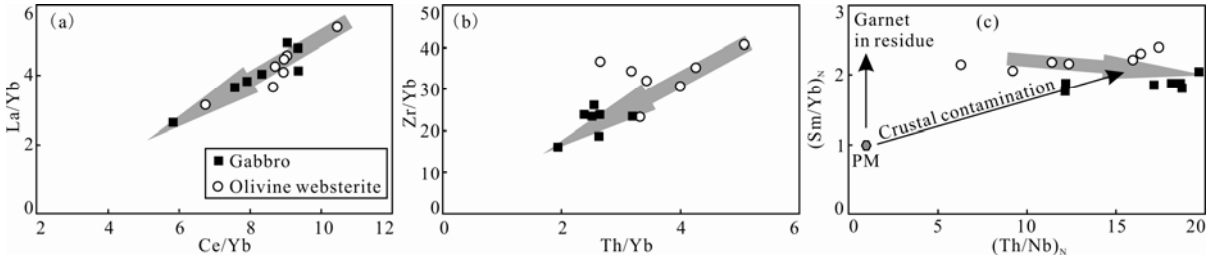

Fig. 11. Ce/Yb vs. La/Yb (a), Th/Yb vs. Zr/Yb (b) and $(La/Nb)_N$ vs. $(Th/Ta)_N$ (c) diagrams of the mafic-ultramafic rocks in the No. I complex.

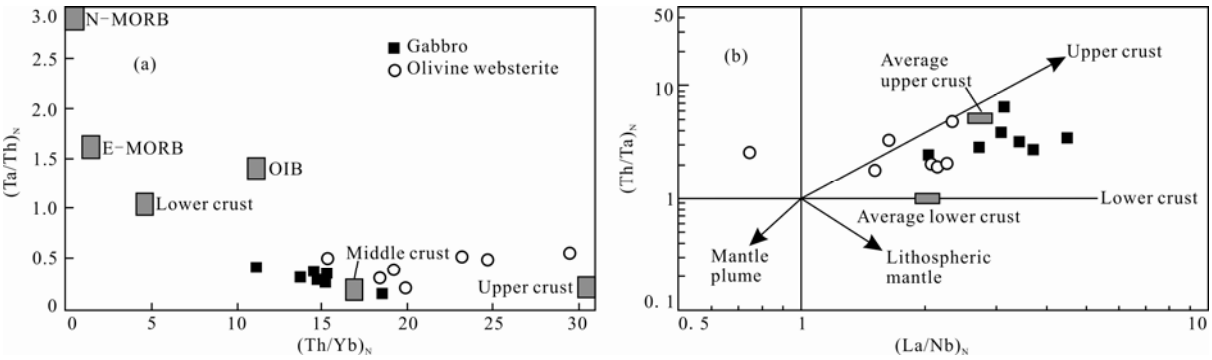

Fig. 12. $(Th/Yb)_N$ vs. $(Ta/Th)_N$ (a) and $(La/Nb)_N$ vs. $(Th/Ta)_N$ (b) diagrams of the mafic-ultramafic rocks in the No. I complex.

mainly originated from the middle crust. The similar phenomena also took place in other complexes associated with magmatic sulfide deposits, such as Voisey's Bay in Canada (Li et al., 2000), Jinchuan in Gansu Province of China (Li and Ripley, 2011), and Xiarihamu in Qinghai Province of China (Wang Guan et al., 2014a; Peng et al., 2016).

The mafic-ultramafic rocks in No. I complex show the geochemistry of enrichments of LREE and LILE (e.g., Rb, Th, K), depletions of HREE and HFSE (e.g., Nb, Ta, Ti, and Zr), and relatively high Th/Yb values (1.40–4.41), and typical arc-like geochemical features (Deng Yufeng et al., 2011), indicate that the source of the magma was affected by subduction-related fluids or melts (Pearce and Peate,1995; Zhao Yun et al., 2016). On the diagram of Nb/Yb vs. Th/Yb (Fig. 13a), these samples plot in the volcanic arc array, reflecting the influence of subduction components. In addition, their Nb/Tb (2.0–7.0) and Zr/Hf (14.1–32.8) values are significantly lower than those of primitive mantle (17.8 and 37, respectively; McDonough and Sun, 1995) and crust (11 and 33 respectively; Taylor and Mclennan, 1985), which, together with the relationships between Th/Nb–Ba/Th and Th/Zr–Nb/Zr (Fig. 13b–c), suggest that the mantle was metasomatized by fluids derived from dehydration of a subducted plate. The above characteristics indicate that a great amount of fluid was injected into the magmatic mantle source (Woodhead et al., 2001; Hanyu et al., 2006; Li Zhuang et al., 2016). Previous studiers have shown that the geochemical composition of mantle magmatic sources in subduction environments was affected by the interaction between mantle peridotite and fluids or melts released during the alteration of oceanic crust, or subduction zone sediments (Hanyu et al., 2006; Tian et al., 2011). As a result, rutile, ilmenite, sphene, and other titanium-bearing minerals have a wide range of Nb, Ta, and Ti distribution

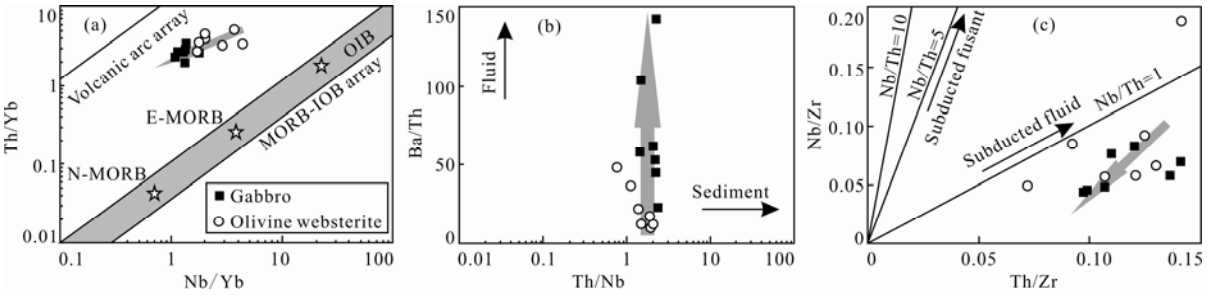

Fig. 13. Nb/Yb vs. Th/Yb (a) and Th/Nb vs. Ba/Th (b) and Th/Zr vs. Nb/Zr (c) diagrams of the mafic-ultramafic rocks in the No. I complex.

coefficients, and fluids derived from the dehydration of oceanic crust are relatively enriched in LILE and depleted in HFSE. These fluids interact with mantle material, enriching it in LILE and further depleting it in HFSE (Stolz et al., 1996; Wang Guan et al., 2014a). In conclusion, we consider that the primary magmas associated with the Shitoukengde magmatic sulfide deposit were originated from a metasomatised, asthenospheric mantle source which had previously been modified by subduction-related fluids.

6.2 Tectonic setting

The Shitoukengde Ni-Cu deposit is located in the basement uplifting and granite belt of middle of Eastern Kunlun, being one part of the Proto-Tethys Ocean tectonic domain. A large igneous province named Wanbaogou OBP (Sun Fengyue et al., 2009) formed on the Pre-Proto Tethys Ocean in late Mesoproterozoic-early Neoproterozoic (Sun Fengyue et al., 2009; Jin Lijie et al., 2015). Like the Ontong Java OBP on the western Pacific, which is the greatest large igneous province in the world recently, Wanbaogou OBP have great thickness of 25–35 km. So it is difficult to subduct beneath the continental crust unlike other normal oceanic plate. Many researches suggest that the Proto-Tethys Ocean opened and expanded due to the rifting and prolonged break-up of Rodinia supercontinent at about 860–570 Ma (Li et al., 2008; Lu Songnian, 2001). Subsequently, the southern margin of Qaidam Block translated from passive continental margin into active continental margin resulting in the trench-arc-basin system in early Caledonian, and the present North Kunlun terranes was the back-arc rift belt at Caledonian. Meanwhile, the Wanbaogou OBP moved toward the Qaidam Block.

A series of ophiolitic melange which distributed along the Middle Kunlun Fault were interpreted as the relic of Proto-Tethys Ocean closure, many mafic rocks of which formed at 522–509 Ma (Yang et al. 1996; Feng Jianyun et al., 2010). With subduction northward of the Proto-Tethys Ocean, a series of arc igneous rocks formed in the southern margin of Qaidam Block. The Kekesha quartz diorite from eastern of BGMK yields an emplaced age of 515 ± 4 Ma and it was regarded as the subduction product of the Proto-Tethys Oceanic plate in early stage (Zhang Yafeng et al., 2010). Zheng Yong et al. (2016) obtained the zircon U-Pb age of Bashikangkuole gabbro which was located in the Qiman Tagh area of 501 ± 1 Ma and suggested it formed in the back-arc basin setting. Volcanic -magma arc belt including different kinds of basic-acid magmatic rocks related to the early Paleozoic subduction of oceanic crust formed in Qiman Tagh area, such as the Yaziquan gabbro and diorite (480 ± 3 Ma; Cui Meihui et al., 2011), Kuangou-Xiaolangyashan basalt and rhyolite (440 ± 2 Ma and 450 ± 1.2 Ma; Wang Bingzhang et al., 2012) and Bashierxi granite (458 ± 9 Ma; Gao Xiaofeng et al., 2010). Consequently, the Baiganhu flysch basin formed due to the back-arc extension in Silurian (Li Guochen et al., 2012). Moreover, gabbro from Qingshuiquan area (452 ± 5 Ma; Sang Jizhen et al., 2016), meta-lava near Dulan County (448 ± 4 Ma; Chen Nengsong et al., 2002) and granodiorite from Gouli area (454 ± 2 Ma; Chen Jiajie et al., 2016) were the responsive product of the subduction northward of the Proto-Tethys Oceanic plate in the eastern part.

Mo Xuanxue et al., (2007) considered the Ar-Ar age (445 Ma) of glaucophane schist from Tumuleke, Qiman Tagh area, as the beginning of collision. Meanwhile, Wang Xiaoxia et al. (2012) and Wang Tao et al. (2016) suggested that the Wanbaogou rapakivi granite (441 ± 5 Ma) and Wulonggou granite (438 ± 3 Ma) formed in the syn-collisional/conversion of syn-collision and post-collision setting. A series of granites in Baiganhu Wu-Sn orefield (430–414 Ma; Gao Yongbao and Li Wenyuan, 2011; Li Guochen et al., 2012; Wang Zengzhen et al., 2014; Zhou Jianhou et al., 2015; Zheng Zhen et al., 2016), including a strongly peraluminous S-type granite, a high-K calc-alkaline I-type granite and a post-orogenic A_2-type granite, were considered forming in the tectonic setting of post-collision and within-plate. The late Ordovician lava located near Dulan County yielded a ^{40}Ar-^{39}Ar plateau age of hornblende with metamorphic origin of 427 ± 4 Ma and represent the metamorphic peak timing of orogenic process (Chen Nengsong et al., 2002). Gao Xiaofeng et al. (2010) obtained the Bashierxi K-feldspar granite with characteristics of A-type granite zircon U-Pb age of 432 ± 1 Ma and suggested that it was the product of the post-collision extensional setting. What's more, Ayak monzonitic granite in Qiman Tagh Mountain (420 ± 4 Ma; Hao Jie et al., 2003) and Houtougou monzogranite in Wulonggou area (Yan Wei et al., 2016) contained the characteristics of typical post-orogenic granite and was considered forming in the post-collision extensional setting. Coexistence of mafic-ultramfic rocks and granites implies that the tectonic regime of Eastern Kunlun Orogen had significantly shifted from syn-collisional extrusion turning into post-collisional extension setting with the intense crust-mantle interaction (Wang Guan et al., 2014a). Last but not least, the large-scale magmatic Ni-(Cu) sulfide deposit associated with the mafic-ultramafic intrusions (394–439 Ma; Li Shijin et al., 2012; Wang Guan et al., 2014a; Jiang Changyi et al., 2015; Li et al., 2015; Peng et al., 2016; Song et al., 2016) was the most significant support for intense extensional setting with the typical post-orogenic A_2-type granite in Xiarihamu area

forming at 391 ± 1 Ma (Wang Guan et al., 2014b). Collectively, these geological evidences indicate that Proto-Tethys Ocean has close before ~445 Ma and then got into the syn-collisional stage (445–438 Ma), and after a post-collision extensional stage.

Zircons selected from the olivine websterite in No. I complex show the characteristics of zircons from basic intrusion, which U-Pb age were obtained by 422 Ma, indicates that Shitoukengde Ni-Cu deposit formed in late Silurian, approximate to the Xiarihamu Ni-(Cu) deposit (394–439 Ma; Li Shijin et al., 2012; Wang Guan et al., 2014a; Jiang Changyi et al., 2015; Li et al., 2015; Peng et al., 2016; Song et al., 2016). This suggests that the strong mafic-ultramafic magma activities associated with Ni-Cu mineralization took place at late Caledonian-early Hercymian epoch in the Eastern Kunlun Orogen, and to be the most significant ore-forming event of magmatic sulfide deposits in this area recently. Many researchers (Aldanmaz et al., 2000; Wang et al., 2004) considered that magmas formed in a post-collisional extensional setting may have geochemical signatures of an island arc or active continental margin. Thus, the source region can retain the characteristics of previously subducted oceanic crust, such as a strong enrichment in LILE (e.g., Rb, Ba, Th, U, and K) and depletions in HFSE (e.g., Nb, Ta, P, and Ti). In conclusion, the Shitoukengde mafic-ultramafic complexes probably formed in a post-collisional and extensional regime, the same as to the Xiarihamu Ni-(Cu) deposit.

6.3 Constraints on ore genesis

Magmatic Cu-Ni-(PGE) sulfide deposit is closely related to the coexistent mafic-ultramafic complex frequently and the mineralization was generally hosted in the ultramafic rocks. Sulfide liquids are enriched in chalcophile elements that become differentiated due to gravitational sinking, leading to sulfide enrichment and mineralization. The forming of large-scale magmatic sulfide deposit was often constrained by the following factors (Naldrett, 1999): a) enough ore-forming material (e.g., Ni, Cu, and PGE); b) attainment of sulphur saturation in magmas; c) plenitudinous reaction between the liquated sulphur and magmas in order to extract abundant Ni; d) accumulation in particular position for sulfides, otherwise low possibility for giant and rich deposit, or even non-ore. Tang Zhongli et al. (1991, 2006) suggested that the liquation and preenrichment of sulfide chiefly finished in the chamber and during ascent, and then these sulfides emplaced to the existent place. The chemical activity and solubility of sulphur, geochemistry of metallogenic element are the most obvious and direct indexes for the study of magmatic sulfide deposit. Because the most important factor for sulfide deposition is the attainment of S saturation in magmas (Brugmann et al., 1993; Mavrogenes and O'Neill, 1999). A negative correlation exists between solubility and magma pressure: S tends to become unsaturated as magma pressure decreases during ascent (Peng et al., 2016). Without external influences, magmatic sulfur cannot generate the saturation which is required to form large-scale deposit (Naldrett, 2004). Assimilation, contamination (especially the felsic contamination) and carbonaceous from country rock, resulting in addition of S and Si, are the key factors for the S saturation in magmas, particularly the intense contamination of crustal material approved by numbers of isotopes, rare earth elements and trace elements (Naldrett, 1999). The $\delta^{34}S$ values of sulfides from No. I complex have a small range of 1.9–4.3 ‰ that slightly greater than mantle $\delta^{34}S$ values (0±2‰; Ripley and Li, 2007), suggesting that magmas that fed the Shitoukengde intrusions assimilated crust-derived S, which was responsible for generating S saturation.

As mentioned above, the mafic-ultramafic rocks from No. I complex have the geochemical signatures of an island arc or active continental margin, such as a enrichment in LREE and LILE (e.g., Rb, Ba, Th, U, and K), depletion in HREE and HFSE (e.g., Nb, Ta, P, and Ti), and its magmatic source was depleted mantle source reformed by subducted fluids. However, complexes in Shitoukengde have great differences to Alaskan-type intrusion on geology, mineralogy, petrology and chemistry. The parental magma of typical Alaskan-type intrusion are generally characterized by CO_2, H_2O-rich fluid , high CaO content and high CaO/Al_2O_3 values (Green et al., 2004; Tian et al., 2011), and the rock-forming minerals mainly are olivine, clinopyroxene and hornblende with minor plagioclase and orthopyroxene, and rocks mainly are dunite, clinopyroxene peridotite, clinopyroxenite and hornblendite (Himmelberg and Loney, 1995; Tian et al., 2011), and the content of magnetite reach 10%–20% commonly (Gu Lianxing et al., 1994). However, the complex in Shitoukengde mainly comprise olivine, orthopyroxene, clinopyroxene and plagioclase on minerals, peridotite, harzburgite, websterite, orthopyroxenite and gabbro on rocks with little magnetite. Thus, we suggest that Shitoukengde is a magmatic Ni-Cu sulfide deposit formed in a post-collisional and extensional regime. Because magmas formed in a post-collisional extensional setting may have geochemical signatures of an island arc or active continental margin (Aldanmaz et al., 2000; Wang et al., 2004).

During subduction northward of the Proto-Tethys Oceanic plate in Early Paleozoic, the subcontinental lithospheric mantle was metasomatic by fluids derived

from dehydration of the subducted oceanic crust resulting in forming enriched lithospheric mantle. Meanwhile, the Wanbaogou OBP moved toward the Qaidam Block. Then (445–438 Ma) the Wanbaogou OBP, as a "soft basement", collaged to the southern margin of Qaidam Block resulting in the closure of Proto-Tethys Ocean. The subduction of the superficial oceanic crust was impeded due to its great thickness (25–35 km), whereas the oceanic crust in deep still keep downgoing. Thus, the subducted oceanic crust certainly break-out due to the asymmetrical pulling force and slab window formed. The suboceanic asthenospheric mantle passed through the slab window and upwelled, which led to partial decompression melting, and the primitive magmas were contaminated with some enriched lithospheric mantle during ascent that formed in the early subduction stage. The fractional crystallization and contamination of generous crustal material in the magma chamber resulted in S saturation and sulfide liquation, and the parental magmas liquated into ore-free magma, ore-bearing magma, ore-rich magma and ore magma. These differentiated magmas pulsatorily emplaced to the crust due to their buoyance, and eventually formed the mafic-ultramafic complexes and Ni-Cu deposit (Fig. 14).

7 Conclusions

(1) The Shitoukengde magmatic Ni-Cu sulfide deposit formed in the late Silurian (426–422 Ma) post-collisional, extensional regime related to the subducted oceanic slab break-off after the Wanbaogou oceanic basalt plateau collaged northward to the Qaidam Block.

(2) The primary magmas were originated from a metasomatised, asthenospheric mantle source which had previously been modified by subduction-related fluids, and experienced significant crustal contamination both in the magma chamber and during ascent triggering S oversaturation by addition of S and Si, that resulted in the deposition and enrichment of sulfides.

Acknowledgements

We thank the staff of the State Key Laboratory of Geological Processes and Mineral Resources, China University of Geosciences, Wuhan, China, Key laboratory of Mineral Resources Evaluation in Northeast Asia, Ministry of Land and Resources of China, MLR Key Laboratory of Metallogeny and Mineral Assessment, Institute of Mineral Resources, Chinese Academy of

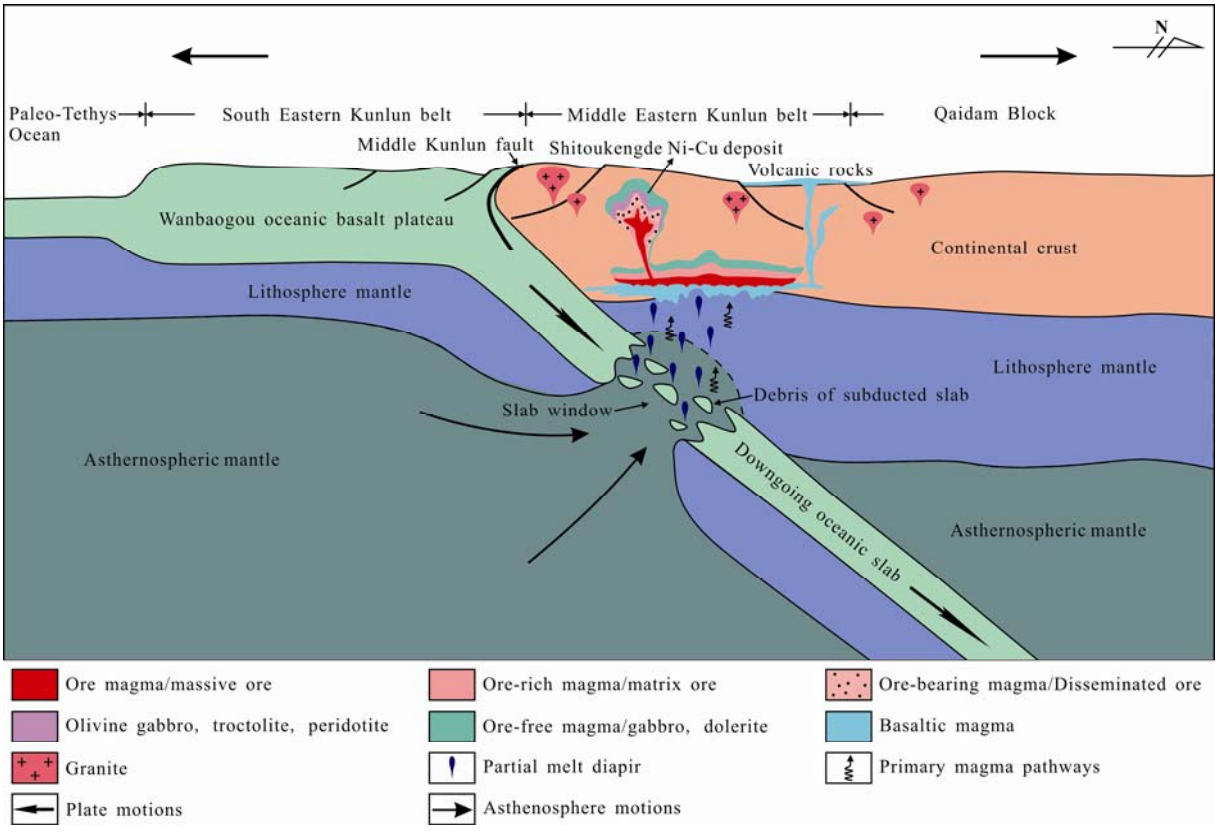

Fig. 14. Diagrammatic sketch of geodynamic process forming the Shitoukengde Ni-Cu deposit in Silurian-Devonian, Eastern Kunlun Orogen (modified from Li Shijin et al., 2012; Barnes et al., 2017).

Geological Sciences, for helping in the analysis. This work was financially supported by the National Natural Science Foundation of China (No. 41272093), and China geological survey project (No. 12120114080901).

Manuscript recived Dec. 2, 2016
accepted May 8, 2017
edited by Fei Hongcai

References

Aldanmaz, E., Pearce, J.A., Thirlwall, M.F., and Mitchell, J.G., 2000. Petrogenetic evolution of late Cenozoic, post-collision volcanism in western Anatolia, Turkey. *Journal of Volcanology and Geothermal Research*, 102 (1–2): 67–95.

Baker, J.A., Menzies, M.A., Thirlwall, M.F., and MacPherson, C.G., 1997. Petrogenesis of Quaternary intraplate volcanism, Sana'a, Yemen: implications for plume-lithosphere interaction and polybaric melt hybridization. *Journal of Petrology*, 38 (10): 1359–1390.

Barnes, S.J., Holwell, D.A., and Vaillant, M.L., 2017. Magmatic sulfide ore deposits. *Elements*, 13: 89–95.

Brugmann, G.E., Naldrett, A.J., Asif, M., Lightfoot, P.C., Gorbachev, N.S., and Fedorenko, V.A., 1993. Siderophile and chalcophile metals as tracers of the evolution of the Siberian traps in the Noril'sk region, Russia. *Geochimica et Cosmochimica Acta*, 57: 2001–2018.

Chen Jiajie, Fu Lebing, Wei Junhao, Tian Ning, Xiong Le, Zhao Yujing, Zhang Yujie and Qi Yueqing, 2016. Geochemical characteristics of late Ordovician granodiorite in Gouli area, Eastern Kunlun Orogenic Belt, Qinghai Province: Implications on the evolution on Proto-Tethys Ocean. *Earth Science*, 41(11): 1863–1882 (in Chinese with English abstract).

Chen Nengsong, He Lei, Sun Min, Wang Guocan and Zhang Kexin, 2002. Precise age limit of Early Paleozoic orogenic metamorphism and thrust deformation, East Kunlun. *Chinese Science Bulletin*, 47(8): 628–631 (in Chinese).

Cui Meihui, Meng Fancong and Wu Xiangke, 2011. Early Ordovician island arc of Qimantg Mountain, eastern Kunlun: Evidences from geochemistry, Sm-Nd isotope and geochronology of intermediate-basic igneous rocks. *Acta Petrologica Sinica*, 27(11): 3365–3379 (in Chinese with English abstract).

Deng Yufeng, Song Xieyan, Chen Liemeng, Cheng Songlin, Zhang Xinli and Li Jun, 2011. Features of the mantle source of the Huangshanxi Ni-Cu sulfide-bearing mafic-ultramafic intrusion, eastern Tianshan. *Acta Petrologica Sinica*, 27(12): 3640–3652 (in Chinese with English abstract).

Feng Jianyun, Pei Xianzhi, Yu Shulun, Ding Saping, Li Ruibao, Sun Yu, Zhang Yafeng, Li Zuochen, Chen Youxin, Zhang Xiaofei and Chen Guochao, 2010. The discovery of the mafic -ultramafic melange in Kekesha area of Dulan County, East Kunlun region, and its LA-ICP-MS zircon U-Pb age. *Geology in China*, 37(1): 28–38 (in Chinese with English abstract).

Fu Piaoer, Tang Qingyan, Zhang Mingjie, Zhang Zhaowei, Li Liwu and Li Wenyuan, 2012. Ore genesis of Kalatongke Cu-Ni sulfide deposit, Western China: Constraints from volatile chemical and carbon isotopic compositions. *Acta Geologica Sinica* (English Edition), 86(3): 568–578.

Furman, T.Y., Bryce, J.G., Karson, J., and Iotti, A., 2004. East African rift system (EARS) plume structure: insight from quarternary mafic lavas of Turkana, Kenya. *Journal of Petrology*, 45: 1069–1088.

Gao Xiaofeng, Xiao Peixi, Xie Congrui, Fan Liyong, Guo Lei and Xi Rengang, 2010. Zircon LA-ICP-MS U-Pb dating and geological significance of Bashierxi granite in the eastern Kunlun area, China. *Geological Bulletin of China*, 29(7): 1001 –1008 (in Chinese with English abstract).

Gao Yongbao and Li Wenyuan, 2011. Petrogenesis of granites containing gungsten and tin ores in the Baiganhu deposit, Qimantage, NW China: Constraints from petrology, chronology and geochemistry. *Geochemica*, 40(4): 324–336 (in Chinese with English abstract).

Green, D.H., Schmidt, M.W., and Hibberson, W.O., 2004. Island -arc ankaramites: primitive melts from fluxed refractory lherzolitic mantle. *Journal of Petrology*, 45(2): 391–403.

Gu Lianxing, Zhu Jianlin, Guo Jichun, Liao Jinjuan, Yan Zhenfu and Yan Hao, 1994. The east Xinjiang-type mafic-ultramafic complexes in orogenic environments. *Acta Petrologica Sinica*, 10(4): 339–356 (in Chinese with English abstract).

Guo, C.L., Chen, Y.C., Zeng, Z.L., and Lou, F.S., 2012. Petrogenesis of the Xihuashan granites in southeastern China: Constraints from geochemistry and in-situ analysis of zircon U-Pb-Hf-O isotopes. *Lithos*, 148: 209–227.

Hanyu, T., Tatsumi, Y., Nakai, S.I., Chang, Q., Miyazaki, T., Sato, K., Tani, K., Shibata, T., and Yoshida, T., 2006. Contribution of slab melting and slab dehydration to magmatism in the NE Japan arc for the last 25 Myr: Constraints from geochemistry. *Geochemistry, Geophysics, Geosystems*, 7(8): 1–29.

Hao Jie, Liu Xiaohan and Sang Haiqing, 2003. Geochemical characteristics and $^{40}Ar/^{39}Ar$ age of the Ayak adamellite and its tectonic significance in the east Kunlun, Xinjiang. *Acta Petrologica Sinica*, 19(3): 517–522 (in Chinese with English abstract).

Hart, S.R., 1988. Heterogeneous mantle domains: signatures, genesis and mixing chronologies. *Earth and Planetary Science Letters*, 90(3): 273–296.

Himmelberg, G.R., and Loney, R.A., 1995. Characteristics and petrogenesis of Alaskan-type ultramafic-mafic Intrusions, southeastern Alaska. *US Geological Survey*, 1564: 1–47.

Huang Qiangtai, Li Jianfeng, Cai Zhourong, Xia Lianze, Yuan Yajuan, Liu Huichuan and Xia Bin, 2015. Geochemistry, geochronology, Sr-Nd isotopic compositions of Jiang Tso ophiolite in the middle segment of the Bangong-Nujiang suture zone and their geological significance. *Acta Geological Sinica* (English Edition), 89(2): 389–401.

Jacobsen, S.B., and Wasserburg, G.J., 1980. Sm-Nd isotopic evolution of chondrites. *Earth and Planetary Science Letters*, 50: 139–155.

Jiang Changyi, Ling Jinlan, Zhou Wei, Du Wei, Wang Zixi, Fan Yazhou, Song Yanfang and Song Zhongbao, 2015. Petrogenesis of the Xiarihamu Ni-bearing layered mafic-ultramafic intrusion, East Kunlun: Implications for its extensional island arc environment. *Acta Petrologica Sinica*, 31(4): 1117–1136 (in Chinese with English abstract).

Jiao Jiangang, Tang Zhongli, Qian Zhuangzhi, Sun Tao, Duan Jun and Jiang Chao, 2012. Genesis and metallogenic Process of Tulaergen large scale Cu-Ni sulfide deposit in eastern Tianshan area, Xinjiang. *Acta Petrologica Sinica*, 28(11): 3772–3786 (in Chinese with English abstract).

Jin Lijie, Zhou Hanwen, Zhu Yunhai and Lin Qixiang, 2015. U-Pb age of the detrital zircon from the Serteng Formation in East Kunlun: Constraints on its provenance and formation time. *Geotectonica et Metallogenia*, 39(4): 691–703 (in Chinese with English abstract).

Li, C.S., and Naldrett, A.J., 2000. Melting reactions of gneissic inclusions with enclosing magma at Voisey's Bay, Labrador, Canada: implications with respect to ore genesis. *Economic Geology*, 95(4): 801–814.

Li, C.S., and Ripley, E.M., 2011. The giant Jinchuan Ni-Cu-(PGE) deposits: tectonic setting, magma evolution, ore genesis and exploration implications. *Reviews in Economic Geology*, 17: 163–180.

Li, C.S., Zhang, Z.W., Li, W.Y., and Ripley, E.M., 2015. Geochronology, petrology and Hf-S isotopes of the newly-discovered, world-class Xiarihamu magmatic Ni-Cu deposit in the Qinghai-Tibet Plateau, western China. *Lithos*, 216–217: 224–240.

Li Guochen, Feng Chengyou, Wang Ruijiang, Ma Shengchao, Li Hongmao and Zhou Anshun, 2012. SIMS zircon U-Pb age, petrochemistry and tectonic implications of granitoids in Northeastern Baiganhu W-Sn orefield, Xinjiang. *Acta Geoscientica Sinica*, 33(2): 216–226 (in Chinese with English abstract).

Li Shijin, Sun Fengyue, Gao Yongwang, Zhao Junwei, Li Liansong and Yang Qi'an, 2012. The theoretical guidance and the practice of small intrusions forming large deposits: The enlightenment and significance for searching breakthrough of Cu-Ni sulfide deposit in Xiarihamu, East Kunlun, Qinghai. *Northwestern Geology*, 45(4): 185–191 (in Chinese with English abstract).

Li Zhuang, Chen Bin and Wang Jialin, 2016. Geochronology framework and geodynamic implications of mafic magmatism in the Liaodong Peninsula and adjacent regions, North China Craton. *Acta Geologica Sinica* (English Edition), 90(1): 138–153.

Li, Z.X., Bogdanova, S.V., Collins, A.S., Davidson, A., De Waele, B., Ernst, R.E., Fitzsimons, I.C.W., Fuck, A., Gladkochub, D.P., Jacobs, J., Karlstrom, K.E., Lu, S., Natapov, L.M., Pease, V., Pisarevsky, S.A., Thrane, K., and Vernikovsky, V., 2008. Assembly, configuration, and break-up history of Rodinia: A synthesis. *Precambrian Research*, 160: 179–210.

Lu Linsu, Mao Jingwen, Zhou Zhenhua, Li Hongbo, Zhang Zuoheng and Wang Yunfeng, 2012. Mineral chemistry of ore-bearing ultramafic rocks from the Hongqiling No. 1 and 7 intrusions in Jilin University: Constraints on the magmatic processes and the metallogenesis of Ni-Cu sulfide deposits. *Acta Petrologica Sinica*, 28(1): 319–344(in Chinese with English abstract).

Lu Songnian, 2001. From Rodinia to Gondwanaland supercontinents–Thinking about problems of researching Neoproterozoic supercontinents. *Earth Science Frontiers* (China University of Geosciences, Beijing), 8(4): 441–448 (in Chinese with English abstract).

Macdonald, R., Rogers, N.W., Fitton, J.G., Black, S., and Smith, M., 2001. Plume-lithosphere interactions in the generation of the basalts of the Kenya Rift, East Africa. *Journal of Petrology*, 42(5): 877–900.

Mavrogenes, J.A., and O'Neill, H.S., 1999. The relative effects of pressure, temperature and oxygen fugacity on the solubility of sulfide in mafic magmas. *Geochimica et Cosmochimica Acta*, 63(7/8): 1173–1180.

McDonough, W.F., and Sun, S.S., 1995. The composition of the earth. *Chemical Geology*, 120: 233–253.

Menzies, M.A., 1989. Cratonic, circumcratonic and oceanic mantle domains beneath the Western United States. *Journal of Geophysical Research*, 94(6): 7899–7915.

Mir, A.R., Alvi, S.H., and Balaram, V., 2011. Geochemistry of the mafic dykes in parts of the Singhbhum granitoid complex: Petrogenesis and tectonic setting. *Arabian Journal of Geosciences*, 4(5–6): 933–943.

Mo Xuanxue, Luo Zhaohua, Deng Jinfu, Yu Xuehui, Liu Chengdong, Chen Hongwei, Yuan Wanming and Liu Yunhua, 2007. Granitoids and crustal growth in the East-Kunlun Orogenic Belt. *Geological Journal of China University*, 13(3): 403–414 (in Chinese with English abstract).

Naldrett, A.J., 1999. World-class Ni-Cu-PGE deposits: key factors in their genesis. *Mineral Deposita*, 34: 227–240.

Naldrett, A.J., 2004. *Magmatic sulfide deposits*. Springer, Berlin, 727.

Ni Zhiyao, 1991. Chemical, composition and petrologic significance of olivines in Huangshandong mafic-ultramafic complex in Hami, Xinjiang, China. *Mineralogy and Petrology*, 11(3): 40–47 (in Chinese with English abstract).

Pearce, J.A., and Peate, D.W., 1995. Tectonic implications of the composition of volcanic arc magmas. Annual *Review of Earth and Planetary Sciences*, 23(1): 251–285.

Peng, B., Sun, F.Y., Li, B.L., Wang, G., Li, S.J., Zhao, T.F., Li, L., and Zhi, Y.B., 2015. The geochemistry and geochronology of the Xiarihamu II mafic-ultramafic complex, Eastern Kunlun, Qinghai Province, China: Implications for the genesis of magmatic Ni-Cu sulfide deposits. *Ore Geology Reviews*, 73: 13–28.

Qian Xin, Feng Qinglai, Wang Yuejun and Zhang Zhibin, 2016. Geochemical and geochronological constraints on the origin of the meta-basic volcanic rocks in the Tengtiaohe Zone, Southern Yunnan. *Acta Geological Sinica* (English Edition), 90(2): 669–683.

Ripley, E.M., and Li, C.S., 2007. Applications of stable and radiogenic isotopes to magmatic Cu-Ni-PGE deposits: examples and cautions. *Earth Science Frontiers*, 14(5): 124–131 (in Chinese with English abstract).

Sang Jizhen, Pei Xianzhi, Li Ruibao, Liu Chengjun, Chen Youxin, Li Zuochen, Chen Guochao, Yang Sen, Wang Xubin, Chen Gong and Deng Wenbing, 2016. LA-ICP-MS zircon U-Pb dating and geochemical characteristics of gabbro in Qingshuiquan, east section of East Kunlun, and its tectonic significance. *Geological Bulletin of China*, 35(5): 700–710 (in Chinese with English abstract).

Saunders, A.D., Norry, M.J., and Tarney, J., 1988. Origin of MORB and chemically-depleted mantle reservoirs: Trace element constraints. *Journal of Petrology*, Special Lithosphere Issue, 415–445.

Song, X.Y., Yi, J.N., Chen, L.M., She, Y.W., Liu, C.Z., Dang, X.Y., Yang, Q.A., and Wu, S.K., 2016. The giant Xiarihamu Ni-Co sulfide deposit in the East Kunlun Orogenic Belt, Northern Tibet Plateau, China. *Economic Geology*, 111: 29–55.

Stolz, A.J., Jochum, K.P., Spettel, B., and Hofmann, A.W., 1996. Fluid-and melt-related enrichment in the subarc mantle: evidence from Nb/Ta variations in island-arc basalts. *Geology*,

24(7): 587–590.

Sun Fengyue, Li Bile, Ding Qingfeng, Zhao Junwei, Pan Tong, Yu Xiaofei, Wang Li, Chen Guangjun and Ding Zhengjiang, 2009. *Research on the key problems of ore prospecting in the Eastern Kunlun metallogenic belt*. Geological Survey Institute of Jilin University, Changchun. 35–57 (in Chinese).

Sun He, Qin Kezhang, Li Jinxiang, Xu Xingwang, San Jinzhu, Ding Kuishou, Hui Weidong and Xu Yingxia, 2006. Petrographic and geochemical characteristics of the Tulargen Cu-Ni-Co sulfide deposit, East Tianshan, Xinjiang, and its tectonic setting. *Geology in China*, 33(3): 606–617 (in Chinese with English abstract).

Sun, S.S., and MacDonough, W.F., 1989. Chemical and isotopic systematics of oceanic basalts: implications for mantle composition and processes. In: Saunders, A.D., and Norry, M.J. (eds.), *Magmatism in the Oceanic Basins*. Geological Society Special Publication, London, 42: 313–345.

Tang, J., Xu, W.L., Wang, F., Wang, W., Xu, M.J., and Zhang, Y.H., 2014. Geochronology and geochemistry of Early-Middle Triassic magmatism in the Erguna Massif, NE China: Constraints on the tectonic evolution of the Mongol-Okhotsk Ocean. *Lithos*, 184–187: 1–16.

Tang Zhongli and Li Wenyuan, 1991. Studies of metallogenic regularity of nickel sulfide deposits in China and their prospects. *Mineral Deposits*, 10(3): 193–203 (in Chinese with English abstract).

Tang Zhongli, Yan Haiqing, Jiao Jiangang and Li Xiaohu, 2006. New classification of magmatic sulfide deposits in China and ore-forming process of small intrusive bodies. *Mineral Deposits*, 25(1): 1–9 (in Chinese with English abstract).

Tang Zhongli, Yan Haiqing, Jiao Jiangang and Pan Zhenxing, 2007. Regional metallogenic controls of small intrusion hosted Ni-Cu (PGE) ore deposits in China. *Earth Science Frontiers*, 14(5): 92–103 (in Chinese with English abstract).

Taylor, S.R., and Mclennan, S.M., 1985. *The continental crust: its composition and evolution*. London: Blackwell, 57–72.

Tian, L.Y., Castillo, P.R., Hilton, D.R., Hawkins, J.W., Hanan, B.B., and Pietruszka, A.J., 2011. Major and trace element and Sr–Nd isotope signatures of the northern Lau Basin lavas: Implications for the composition and dynamics of the back-arc mantle. *Journal of Geophysical Research*, 116(B11): 148–151.

Wang Bingzhang, Luo Zhaohua, Pan Tong, Song Taizhong, Xiao Peixi and Zhang Zhiqing, 2012. Petrotectonic assemblages and LA-ICP-MS zircon U-Pb age of Early Paleozoic volcanic rocks in Qimantag area, Tibetan Plateau. *Geological Bulletin of China*, 31(6): 860–874 (in Chinese with English abstract).

Wang Chongyi, Shi Changyun and Wang Xiaoting, 1986. Primary study of diagenetic process of Huangshan basic-ultrabasic rock body and its ore-bearing Charactors. *Xinjiang Geology*, 4(1): 1–11 (in Chinese with English abstract).

Wang Guan, Sun Fengyue, Li Bile, Li Shijin, Zhao Junwei, Ao Cong and Yang Qi'an, 2014a. Petrography, zircon U-Pb geochronology and geochemistry of the mafic-ultramafic intrusion in Xiarihamu Cu-Ni deposit from East Kunlun, with implications for geodynamic setting. *Earth Science Frontiers*, 21(6): 381–401 (in Chinese with English abstract).

Wang Guan, Sun Fengyue, Li Bile, Li Shijin, Zhao Junwei, Yang Qi'an and Ao Cong, 2014b. Zircon U-Pb geochronology and geochemistry of the early Devonian syenogranite in the Xiarihamu ore district from East Kunlun, with implications for the geodynamic setting. *Geotectonica et Metallogenia*, 37 (4): 685–697 (in Chinese with English abstract).

Wang Guan, Sun Fengyue, Li Bile, Ao Cong, Li Shijin, Zhao Junwei and Yang Qi'an, 2016. Geochronology, geochemistry and tectonic implication of early Neoproterozoic monzogranite in Xiarihamu ore district from East Kunlun. *Geotectonica et Metallogenia*, 40(6): 1247–1260 (in Chinese with English abstract).

Wang, K.L., Chung, S.L., O'reilly, S.Y., Sun, S.S., Shinjo, R., and Chen, C.H., 2004. Geochemical constraints for the genesis of post-collisional magmatism and the geodynamic evolution of the Northern Taiwan region. *Journal of Petrology*, 45(5): 975–1011.

Wang Tao, Li Bin, Chen Jing, Wang Jinshou, Li Wufu and Jin Tingting, 2016. Characteristics of chronology and geochemistry of the early Silurian monzogranite in the Wulonggou area, East Kunlun and its geological significance. *Journal of Mineral and Petrology*, 36(2): 62–70 (in Chinese with English abstract).

Wang Xiaoxia, Hu Nenggao, Wang Tao, Sun Yangui, Ju Shengcheng, Lu Xinxiang, Li Shan and Qi Qiuju, 2012. Late Ordovician Wanbaogou granitoid pluton from the southern margin of the Qaidam basin: Zircon SHRIMP U-Pb age, Hf isotope and geochemistry. *Acta Petrologica Sinica*, 28(9): 2950–2962 (in Chinese with English abstract).

Wang Zengzhen, Han Baofu, Feng Chengyou and Li Guochen, 2014. Geochronology, geochemistry and tectonic significance of granites in Baiganhu area, Xinjiang. *Acta Petrologica et Mineralogica*, 33(4): 597–616 (in Chinese with English abstract).

Wei, B., Wang, Y.C., Li, C.S., and Sun, Y.L., 2013. Origin of PGE-deposit Ni-Cu sulfide mineralization in the Triassic Hongqiling No.7 orthopyroxenite intrusion, Central Asian Orogenic Belt, Northeastern China. *Economic Geology,* 108 (8): 1813–1381.

Woodhead, J.D., Hergt, J.M., Davidson. J.P., and Eggins, S.M., 2001. Hafnium isotope evidence for 'conservative'element mobility during subduction zone processes. *Earth and Planetary Science Letters*, 192(3): 331–346.

Wu Fuyuan, Li Xianhua, Zheng Yongfei and Gao Shan, 2007. Lu-Hf isotopic systematics and their applications in petrology. *Acta Petrologica Sinica*, 23(2): 185–220 (in Chinese with English abstract).

Wu, F.Y., Yang, Y.H., Xie, L.W., Yang, J.H., and Xu, P., 2006. Hf isotopic compositions of the standard zircons and baddeleyites used in U-Pb geochronology. *Chemical Geology*, 234: 105–126.

Wu Liren, 1963. Study on the metallogenetic specialization of basic and ultrabasic rocks in China. S*cientia Geologica Sinica*, 1: 29–41 (in Chinese).

Xia Zhaode, Xia Mingzhe and Jiang Changyi, 2017. Geochronology, petrology and geochemistry of Xingdi No. 3 mafic-ultramafic intrusions in the Northeastern Tarim Craton, NW China. *Acta Geologica Sinica* (English Edition), 91(2): 500–514.

Yan Wei, Qiu Dianming, Ding Qingfeng and Liu Fei, 2016. Geochronology, petrogenesis, source and its structural significance of Houtougou monzogranite of Wulonggou area in Eastern Kunlun Orogen. *Journal of Jilin University* (Earth Science Edition), 46(2): 443–460 (in Chinese with English abstract).

Yang, J.S., Robinson, P.T., Jiang, C.F., and Xu, Z.Q., 1996. Ophiolites of the Kunlun Mountains, China and their tectonic implications. *Tectonophsics*, 258: 215–231.

Yang Xin, Xu Xuhui, Zhang Zhongpei, Liu Yifeng, Zhang Jibiao, Liu Xingwang, Xiong Ping and Zheng Jianjing, 2016. Cenozoic magmatism and Tectonic framework of Western Yunnan, China: Constrained from geochemistry, Sr-Nd-Pb isotopes and fission track dating. *Acta Geologica Sinica* (English Edition), 90(5): 1679–1698.

Zhang Yafeng, Pei Xianzhi, Ding Saping, Li Ruibao, Feng Jianyun, Sun Yu, Li Zuochen and Chen Youxin, 2010. LA-ICP-MS zircon U-Pb age of quartz diorite at the Kekesha area of Dulan County, eastern section of the East Kunlun orogenic belt, China and its significance. *Geological Bulletin of China*, 29(1): 79–85 (in Chinese with English abstract).

Zhang Zhaochong, Yan Shenghao, Chen Bailin, He Lixin, He Yongsheng and Zhou Gang, 2003. Geochemistry of the Kalatongke basic complex in Xinjiang and its constraints on genesis of the deposit. *Acta Petrological et Mineralogica*, 22 (3): 217–224 (in Chinese with English abstract).

Zhang, Z.C., Mao, J.W., Chai, F.M., Yan, S.H., and Chen, B.L., 2009a. Geochemistry of the Permian Kalatongke mafic intrusions, Northern Xinjiang, NW China: Implications for the genesis of the magmatic Ni-Cu sulfide deposit. *Economic Geology*, 104(2): 185–203.

Zhang, Z.C., Mao, J.W., Saunders, A.D., Ai, Y., Li, Y., and Zhao, L., 2009b. Petrogenetic modeling of three mafic-ultramafic layered intrusions in the Emeishan large igneous province, SW China, based on isotopic and bulk chemical constraints. *Lithos*, 113(3–4): 369–392.

Zhao, J.H., and Zhou, M.F., 2007. Geochemistry of Neoproterozoic mafic intrusions in the Panzhihua district (Sichuan Province, SW China): Implications for subduction-related metasomatism in the upper mantle. *Precambrian Research*, 152(1): 27–47.

Zhao Yun, Yang Yongqiang and Ke Junjun, 2016. Origin of Cu- and Ni-bearing magma and sulfide saturation mechanism: A case study of Sr-Nd-Pb-S isotopic composition and element geochemistry on the Huangshannan magmatic Ni-Cu sulfide deposit, Xinjiang. *Acta Petrologica Sinica*, 32(7): 2086–2098 (in Chinese with English abstract).

Zheng Yong, Yang Yousheng, Chen Bangxue and Zhu Yanfei, 2016. Geochemical characteristics and tectonic significance of gabbro from Bashikangkuole in west part of Eastern Kunlun, China. *Geoscience*, 30(5): 1004–1013 (in Chinese with English abstract).

Zheng Zhen, Chen Yanjing, Deng Xiaohua, Yue Suwei and Chen Hongjin, 2016. Muscovite ^{40}Ar-^{39}Ar dating of the Baiganhu W-Sn orefield, Qimantag, East Kunlun Mountains, and its geological implications. *Geology in China*, 43(4): 1341–1352 (in Chinese with English abstract).

Zhou Jianhou, Feng Chengyou, Li Daxin, Wang Hui, Zhang Mingyu, Li Guochen and Wang Zengzhen, 2015. Petrology, geochronology and geochemistry of metallogenetic granite in Baiganhu W-Sn deposit, East Kunlun. *Acta Petrologica Sinica*, 31(8): 2277–2293 (in Chinese with English abstract).

Zhou Wei, Du Wei and Wang Zixi, 2015. Geochronology and its significance of the mafic-ultramafic complex in Shitoukengde Cu-Ni mineral occurrence, Eastern Kunlun. *Journal of Jilin University* (Earth Science Edition), 45(sup.1): 1–2 (in Chinese with English abstract).

Zhou Wei, Wang Bangyao, Xia Mingzhe, Xia Zhaode, Jiang Changyi, Dong Jun and Xie Enshun, 2016. Mineralogical characteristics of Shitoukengde mafic-ultramafic intrusion and analysis of its metallogenic potential, East Kunlun. *Acta Petrologica et Mineralogica*, 35(1): 81–96 (in Chinese with English abstract).

About the first author

LI Liang Male; born in 1986 in Yulin City, the Guangxi Zhuang Autonomous Region; a PhD graduate majoring in mineral deposits from College of Earth Sciences, Jilin University now. He has worked in Qinghai Province for eight years and has a rich experience and deep understanding on the basic geological and mineral of Qinghai. He is now carrying out the project of "Research on the metallogenic regularity and ore prospecting of the magmatic Cu-Ni sulfide deposits in the surroundings of Qaidam Basin, Qinghai Province".Address: No. 2199 Jianshe Street, Chaoyang District, Changchun City, Jilin Province, China.E-mail: liliangjlu2011@163.com.